Technische Universität Berlin

Fakultät VI Planen Bauen Umwelt
Institut für Geodäsie und Geoinformationstechnik
Fachgebiet GNSS-Fernerkundung, Navigation und Positionierung

Master Thesis

Airborne GNSS reflectometry for coastal monitoring of sea state

Mario Andrés Moreno Bulla
Matriculation number: 400621

Supervised by:
Prof. Dr. Jens Wickert
Dr. Maximilian Semmling

February 17, 2021, Berlin

Hiermit erkläre ich, dass ich die vorliegende Arbeit selbstständig und eigenhändig sowie ohne unerlaubte fremde Hilfe und ausschließlich unter Verwendung der aufgeführten Quellen und Hilfsmittel angefertigt habe.

Berlin, 17.02.2021

.....

Mario Andrés Moreno Bulla

I hereby declare that I have prepared the present work independently and with my own hands and without unauthorized outside help and exclusively using the sources and resources listed.

Berlin, 17.02.2021

.....

Mario Andrés Moreno Bulla

Abstract

Sea level rise and sea state variability due to climate change and global warming are major research topics in the scientific community. Multiple techniques have been developed to observe and monitor these phenomena with great precision on a global scale. However, these techniques present limitations in terms of spatial and temporal resolution or poor performance in coastal zones, which are highly dynamic complex areas impacted by increasing sea level and wind-wave effects represented by the sea state.

This Master's thesis presents the possibility of using GNSS-Reflectometry (GNSS-R) to monitor sea state in coastal areas. GNSS-R is a bistatic radar-based technique that allows for retrieval of the Earth's surface properties by analyzing direct and reflected signals (once it bounces off the Earth's surface) captured by a receiver. This study relies on, first, the observed minus computed (O-C) reflected signal power from which a sea state factor (SSF) is derived, and second, analysis of the Doppler shift distribution of the reflected signal to then correlate them with ancillary date of wind speed (WS) and significant wave height (SWH) from the ERA5 model. The tracking process of the direct signal allows us to retrieve its power, and a re-tracking process, aided by a signal path model, is used to obtain the power of the reflected signal. Direct and reflected power are used to compute the observed reflectivity reduced by a modeled (computed) reflectivity to calculate the SSF. The Doppler distribution involves the computation of the mean and standard deviation of the Doppler frequency shift. The latter is retrieved from the power spectral density approach computed every minute from the in-phase (I) and quadrature (Q) components of the reflected re-tracked signal.

Results have shown a sensitivity of the sea state factor and the Doppler distribution with respect to ERA5 sea state parameters with dependency on the GNSS satellite elevation angle as well. As the increase in the roughness of the sea surface, there is a loss on the power of the reflected signal. Therefore, the SSF has a high and moderate anti-correlation with respect to WS and SWH at low elevations ($E < 10°$), with values of, -0.73 and -0.51, respectively. The Doppler standard deviation has a high correlation with WS and SWH of 0.94 and 0.85 respectively, decreasing progressively whit the increase in elevation angle.

Zusammenfassung

Der Anstieg des Meeresspiegels und die Veränderung des Seegangs sind nachweisbare Folgen des Klimawandels und der globalen Erwärmung, die in vielen wissenschaftlichen Studien untersucht werden. Es existieren verschiedene Methoden, um diese Phänomene global mit großer Präzision zu beobachten und zu überwachen. Diese Methoden sind jedoch eingeschränkt in der räumlichen und zeitlichen Auflösung bzw. in der küstennahen Anwendung. Küstengebiete sind komplex gegliedert und einer hohen Dynamik des Meeres unterworfen. Sie sind besonders bedroht durch den Anstieg des Meeresspiegels und durch extreme Wetterereignisse.

Diese Masterarbeit bietet die Möglichkeit, mithilfe der GNSS-Reflektometrie (GNSS-R) den Seegang (als Parameter für Extremwetterereignisse) in Küstengebieten zu überwachen. GNSS-R ist eine bi-statische Radarmethode, mit der Oberflächeneigenschaften der Erde abgeleitet werden, indem direkte und reflektierte Signale (nach Reflektion an der Erdoberfläche) von einem Empfänger erfasst und danach analysiert werden. Diese Studie stützt sich zum einen auf Beobachtungen der Signalstärke, aus der ein Seegangsfaktor (SSF) abgeleitet wird, und zum anderen auf die Analyse der Doppler-Verteilung des reflektierten Signals. Die Ergebnisse werden auf Abhängigkeit von Windgeschwindigkeit (WS) und signifikanter Wellenhöhe (SWH) untersucht (unter Nutzung von Zusatzdaten des ERA5-Modells). Die Nachverfolgung des direkten und reflektierten Signals ermöglicht es, die jeweiligen Signalstärken abzuleiten. Im reflektierten Fall wird die Nachverfolgung durch ein Modell des Signalwegs unter-stützt. Die Signalstärken erlauben es das Reflexionsvermögen zu berechnen und dieses durch ein modelliertes Reflexionsvermögen zu reduzieren, um den SSF zu erhalten. Die Doppler-Verteilung (Mittelwert und Standardabweichung) ergibt sich aus Signalspektren, die minütlich aus den In-Phase- (I) und Quadratur- (Q)-Komponenten des reflektierten Signals berechnet werden.

Die Ergebnisse zeigen die Abhängigkeit der beobachteten Größen (Seegangsfator und Dopplerverteilung) von den genannten Zusatzdaten (WS, SWH) und vom Elevationswinkel des GNSS-Satelliten. Mit zunehmender Rauigkeit der Meeresoberfläche geht reflektierte Signalstärke verloren. Der SSF liefert eine hohe und moderate Antikorrelation in Bezug auf WS und SWH mit Werten von -0.75 bzw. -0,51 (bei Elevationswinkeln $<10°$). Die Doppler-Standardabweichung zeigt eine hohe Korrelation mit WS und SWH von 0.94 bzw. 0.85, die mit zunehmendem Elevationswinkel ab-nimmt.

Acknowledgments

I would first like to thank my examination committee, Prof. Dr. Jens Wickert for the continuous support, academic and master's- thesis guidance, and advice that encouraged me to continue exploring geosciences research. And Prof. Dr. Frank Flechtner for his teaching lectures and support in the thesis evaluation process.

I express my deep sense of thanks and gratitude to my mentors and supervisors Dr. Maximilian Semmling and Dr. Georges Stienne since without their valuable help, guidance, and expertise, it would not have been possible to carry out this master's thesis project. To Dr. Semmling, thank you very much for this exciting journey in the academic and research fields, for allowing me to participate from the first moment in this project and for guiding and teaching me from what began as a geodesy seminar topic, the participation in the scientific publication process, until the materialization of this thesis work. To Dr. Stienne, thank you very much for the invaluable contributions, for teaching me with patient and detailed explanations, and for the multiple discussion session to accomplish this research work.

I would also like to thank the Deutsches GeoForschungsZentrum (GFZ) for allowing me to join as an invited researcher to participate in the measurements campaign and provide me the resources to carry out this project, and to the Laboratoire d'Informatique, Signal et Image de la Côte d'Opale (LISIC), Université du Littoral Côte d'Opale (ULCO) also for the cooperation and resources provided throughout the duration of this project.

Besides, I really thank my parents, for always being there for me permanently teaching me that the value of studies is priceless, and to my wife for sharing this thought and accompanying me on this journey of permanent valuable moments.

To my brother and sisters, thank you, it is worth dreaming!

Danke!

Contents

1 Introduction 8
2 Theory and Definitions 13
2.1 Global Navigation Satellite Systems (GNSS) 13
2.1.1 GPS and Electromagnetic Waves 14
2.1.2 GPS Signal Structure 17
2.1.3 Signal Acquisition and Tracking 18
2.2 GNSS Reflectometry 20
2.2.1 Observation Geometry 20
2.2.2 Reflection Process 22
2.2.3 Interferometric Approach 26
2.2.4 Signal Path Model 30
2.3 Sea State Parameters - Ancillary Data 32
3 Flight Experiment and Data Analysis 35
3.1 Study Area Description 35
3.2 Platform and Antenna Set-up 37
3.3 Flight Information and Data Sets 38
3.4 Data Analysis and Processing 41
3.4.1 Reflection Events Analysis 41
3.4.2 Data Processing 43
4 Modeling and Retrievals Results 46
4.1 Signal Path Modeling and Validation 46
4.1.1 Specular point position 46
4.1.2 Modeled Path Difference 49
4.2 Sea State Observation 52
4.2.1 Power Spectral Density 52
4.2.2 Observed Reflectivity 56
4.2.3 Correlation Sea State Factor and Sea State 60
4.2.4 Correlation Doppler Shift and Sea State 65
5 Conclusions and Outlook 69

1 Introduction

Climate change is currently one of the foremost topics of study within many fields in the scientific community. Different studies have been carried out in recent decades to determine the possible risks and hazards, and the impact that they can produce on humans and their environments. About 40% of the global population lives near coastal areas and depends on ocean resources to survive [United Nations, 2017]. Coastal areas are dynamic systems affected by a variety of natural and anthropogenic forces. Multiples studies have focused on the monitoring and analysis of factors that intervene in the coastal zones and their permanent changes in the context of changing climates. Figure 1.1 presents the beach evolution of the coastal barrier in Chatham, MA, USA coast from 1985 to 2020. Due to the rising sea level, the waves, currents, winds, and tides, in addition to human activities, barrier beaches are constantly changing.

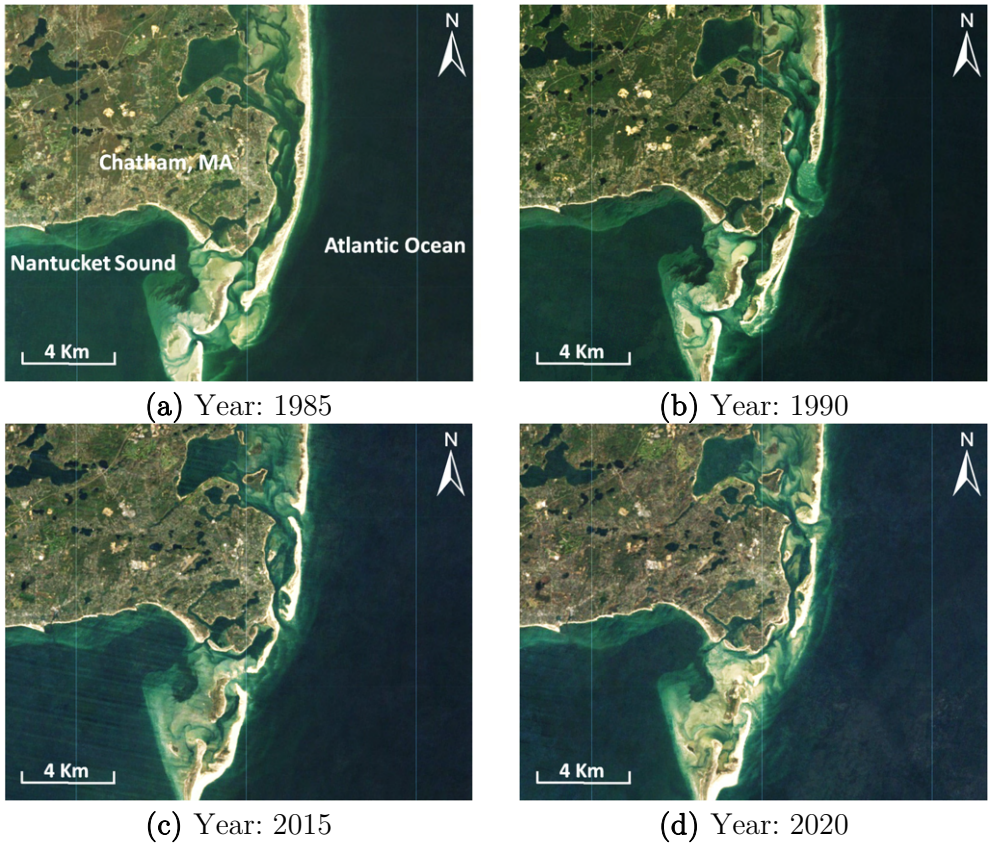

(a) Year: 1985 (b) Year: 1990

(c) Year: 2015 (d) Year: 2020

Figure 1.1: Coastal barrier evolution in Chatham, MA, USA. (a) and (b) Satellite images Landsat 5, (c) image Landsat 7, (d) image Landsat 8.

Sea level variability and change are among the main factors with great human impact. Satellite altimetry enhanced for the open ocean has allowed advances in monitoring this variability globally and regionally. Based on this technology, it has been possible to determine the permanent global mean sea level rising at a rate of 3 mm per year [NASA, 2020]. This effect is primarily caused by global warming, which generates, both thermal expansion due to increasing seawater temperatures and, the melting of sea ice and glaciers, and the loss of the terrestrial ice mass in Greenland and Antarctica [Cazenave & Cozannet, 2014].

The heterogeneity of the sea surface or the presence of slopes makes sea level derivation directly linked to surface roughness. The latter can be interpreted as sea state, another important factor of interest in coastal areas. Sea state is the description of waves generated by the wind, including their height, direction, and period [ESA Climate Office, 2020]. Different authors have pointed out how the wind-wave component can represent considerable changes in sea level along coasts (see [Bengtsson et al., 2006; Melet et al., 2020]). However, techniques for measuring sea level are much more mature than those for detecting winds and waves in coastal areas [Benveniste et al., 2019]. The focus of this thesis is to investigate the possibility of using GNSS-Reflectometry (GNSS-R) from low-altitude airborne measurements campaign, to determine the sensitivity of the phase, power, and Doppler shift observations of the reflected signal to the sea state and establish the correlation between the reflectivity response with wind speed (WS) and significant wave height (SWH). An additional aim is to assess the experimental configuration in terms of the platform used, antenna setup, and flight design.

To monitor ocean parameters, different techniques and sensors exist to measure sea level and identify sea state with high precision and temporality. Tide gauges and buoys are among the sensors that make this task possible. However, their measurements allow only for in-situ observations, so spatial resolution is limited. As mentioned, satellite altimetry is one of the most useful altimetry techniques. However, its drawbacks are due to its temporal resolution (6-12 days), and poor performance in coastal zones due to specific wind-wave influence on the sea surface and the combination of sea waters and land at shorelines [Benveniste et al., 2019]. In the early 1990s, Martín-Neira, [1993] proposed a multi-static radar concept. It consisted of using Global Navigation Satellite Systems (GNSS) signals with an interferometric approach, combining the direct signal with the

signals reflected by the Earth's surface to retrieve the measurements required. Today, this technique is known as GNSS-R and can be used as a complement to the previously mentioned methods, represented in the sketch in Figure 1.2, improving spatial and temporal resolution, and allowing for coastal areas measurement at a global scale.

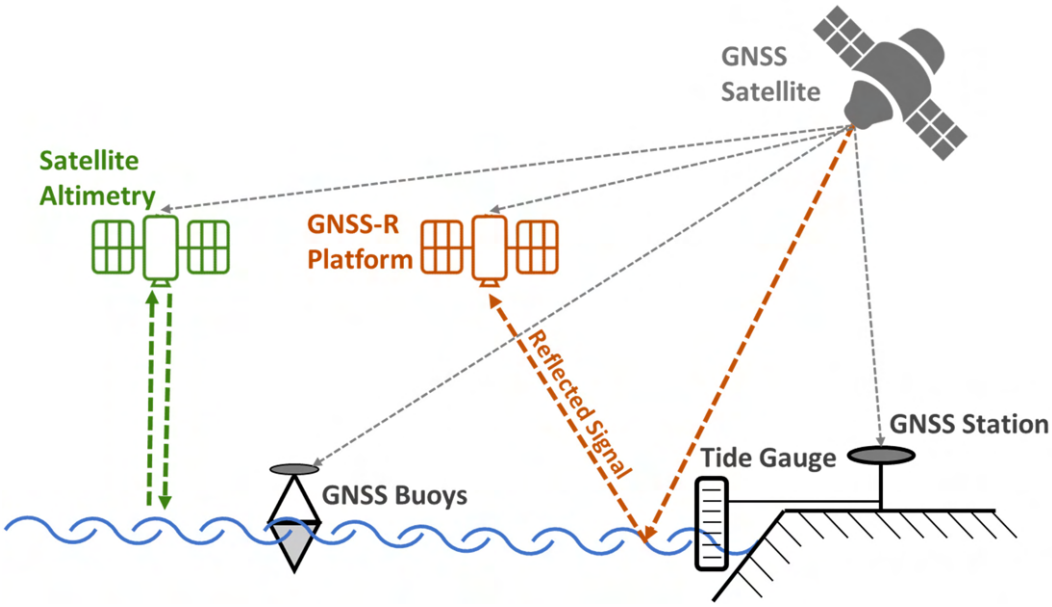

Figure 1.2: Sketch of the ocean monitoring techniques (not to scale). GNSS signals support the different techniques, and the reflected signals could provide information about the sea surface in the open sea and coastal areas.

Reflection process of an electromagnetic wave on a surface can be expressed in terms of two components: specular reflection and diffuse reflection. Normally, this process is a combination of both. When the surface is "smooth" enough, the specular or coherent component will dominate, and the scattering process can be expressed as a function of a well-defined phase [Beckmann & Spizzichino, 1987]. In contrast, the incoherent component will dominate when the surface is "rough" enough and the resulting phase of the scattered ray behaves randomly. In the latter case, the coherency in the reflection process is lost.

Based on these considerations, different experiments have been conducted using GNSS-R to retrieve sea level and sea state (surface roughness), exploring different experimental set-ups and observables. Alonso-Arroyo et al., [2015] utilized a

ground-based (pier) setup with a horizon-looking antenna at a height of ~4.5m. An Interference Pattern Technique (IPT) was used, where the direct and reflected signals are combined to obtain the interference pattern that is visible to the observable: The Signal-to-Noise Ratio (SNR). To determine the SWH and Mean Sea Surface Level (MSSL), it is necessary to identify the point where the coherency in the reflection is lost. Accuracy of 5.7cm and 4.1cm on the SWH and MSSL, respectively, was demonstrated from experimental data. Promising results have been also found using airborne and spaceborne data. A signal path model contribution (based on the excess time of the reflected signal, with respect to direct signal) was used for observations of Sea Surface Topography (SST) utilizing carrier phase data by Semmling et al., [2014]. The platform was a scientific aircraft flying at a high of ~3500 m above sea level. An up-looking antenna and two portside-looking antennas were installed. Centimetric precision on the SST estimation was achieved (δT_{std}<10cm) with elevation angles from the platform between 11° and 33°. Recently, Cardellach et al., [2020] used data collected from the space-borne platform NASA Cyclone GNSS mission (CyGNSS) and demonstrated precisions between 3-4 cm of the sea surface altimetric retrievals under sea state conditions below 6 m/s wind speed and 1.5 m significant wave height. The technique implemented considered Grazing Angles geometry condition (elevation angles up to 25°) and Carrier Phase-delay Altimetry (GA CaPA).

In this project, the measurements campaign was led by the Deutsches GeoForschungsZentrum (GFZ) and the Laboratoire d'Informatique, Signal et Image de la Côte d'Opale (LISIC), Université du Littoral Côte d'Opale (ULCO). It involved a single up-looking GNSS dual-polarized antenna (tilted ~43° with respect to zenith direction) linked to two independent single front-end receivers. This arrangement was aboard of a gyrocopter, a low-altitude, and stable aircraft. The flights were performed in July 2019, about 750m above sea level over the North Sea along the coast between the cities of Calais and Boulogne, France. By using a software receiver, the phase, power, and Doppler shift of the reflected signal are used as observables to retrieve the Doppler distribution (mean and standard deviation) and the sea state factor (SSF). The latter is the difference between the observed reflection power and the specular sea surface reflection model based on Nievinski & Larson, [2014] which is an extension of the model proposed in Zavorotny & Voronovich, [2000] and Zavorotny et al., [2010]. The ERA5 model from the European Centre for Medium-Range Weather Forecasts

(ECMWF) was used to obtain the wind speed and SWH parameters to determine their correlation with the SSF and the Doppler distribution.

This Master thesis has the following structure. In Section 2, it is given an introductory theoretical background and definitions about GNSS, their configuration and observables, the structure of the signals, and the processing for acquiring and tracking them. Besides, it is described the concept of GNSS-R including the signal path and power models utilized to compare with the observed retrievals (observed minus computed, "O-C"). Finally, the description of the ancillary raw data of sea state parameters and the computation of the employed outputs can be found in this section. In Section 3, it is presented the experimental set-up in the airborne coastal experiment will be presented, and described the study area, flight information, and data sets collected can be also found. This section contains the preliminary reflection response analysis utilized to identify the segments and sets of data to be analyzed and the processing steps carried out in this thesis. In Section 4, it is presented the modeling and observation retrievals results from the data captured. The modeling subsection contains the signal path modeling which involves the computation of specular point location and path difference model and validation. The retrievals subsection contains the computation of the sea state factor and Doppler distribution and the results of their correlation with the ancillary data. Finally, conclusions and outlook are given in Section 5. It includes conclusions about the processing steps, analysis of the correlation results, and assessment of the experimental configuration based on the antenna and receiver's set-up, platform, and flight plan design. The outlook subsection describes opportunities for future research and complementary analyzes that can be carried out from this study.

As an additional tool, a free geo-visualizer web application to present evidence of the results of this master's thesis interactively is created. The tool can be accessed via https://reflectometry.herokuapp.com/. It consists of a map-based application with an intuitive and user-friendly interface that allows for the creation of filters to dynamically select the complete data set or subsets of data and visualize results in plots.

2 Theory and Definitions

Nowadays, Global Navigation Satellite Systems are well-designed, stable, and global coverage systems employed for different applications within multiple industries. This has allowed the creation and enhancement of new techniques that use the broadcasted signals not only for navigation, position, and timing but also as a remote sensing tool for Earth observation. This section presents the fundamentals of GNSS, the description of its signals and observables followed by the description of the GNSS-R technique, and the modeling and results from calculation methods used in this Master thesis.

2.1 Global Navigation Satellite Systems (GNSS)

Global Navigation Satellite System is an "all-weather" conditions system that makes available autonomous geospatial positioning with the use of artificial satellite constellation ensuring global coverage. By using time signals transmitted from satellites, an electronic receiver (observer) can determine its Position, Velocity, and Time (PVT). The position is retrieved base on the distances between the observer and different satellites at known locations. This distance is described as pseudorange ρ and is calculated from the travel time of the signal path from the satellite to the observer. Using the speed of light ($c = 299{,}792{,}458\ m/s$), the pseudorange can be written as $\rho = time\ of\ travel \cdot speed\ of\ light$. However, the signal path is influenced by different factors, so the ρ is written as a function of the time delay τ, biased by receiver clock, and its disturbances due to atmospheric delays n_ρ

$$\rho_i = |x_i - x_u| + c\tau + n_{\rho_i} \tag{2.1}$$

Where x_i represent the position vector of satellite i, and x_u the position vector of the observer that is unknown in the equation and as well as the receiver clock bias, τ_{bias}

The Doppler shift can be used as observable to estimate the observer velocity. The Doppler shift is defined as the amount of change in carrier frequency due to the relative motion between a satellite and observer. As the Doppler shift is related to the pseudorange change, it can be expressed as pseudorange rate $\dot{\rho}$

([Ziedan, 2006] eq.(1.6)). Pseudorange rate $\dot{\rho}$ is written in eq. (2.2) where the dot denotes time-derivatives.

$$\dot{\rho}_i = (v_i - v_u) \cdot \frac{x_i - x_u}{|x_i - x_u|} + c\dot{\tau} + n_{\dot{\rho}_i} \tag{2.2}$$

v_i and v_u are the satellite and the observer velocity vectors, respectively. The Doppler shift then is given by, $f_{d_i} = -\dot{\rho}_i/\lambda$, with $\lambda = c/f_L$ where f_L is the carrier frequency.

There are currently different navigation systems continuously evolving and growing, allowing a permanent improvement in the quality and density of signal sources. At the time of this thesis, the existing satellite navigation systems are Global Position System (GPS) operated by the United States Space Force, which currently has 32 satellites (30 operational)[1], the Russian system, GLONASS, with 28 satellites (23 operational)[2], Galileo created by the European Union through the European Space Agency (ESA) with 30 satellites (24 operational)[3], the Chinese system BeiDou with 49 satellites (44 operational)[4], The four-satellite Japanese system Quasi-Zenith Satellite System (QZSS)[5], and NavIC (IRNSS) system operated by the Indian Space Research Organization currently with 8 satellites, all of them operational[6]. This master thesis will focus on the analysis of signals from GPS, so the methods and results presented are based on its signal structure.

2.1.1 GPS and Electromagnetic Waves

Due to its advantageous characteristics, sine or sinusoidal waves are frequently used in different applications including satellite navigation systems. A sinusoidal wave is a curve that describes a smooth repetitive oscillation. Figure 2.1. shows a representation and the components of a sinusoidal wave in time domain t,

---

Constellation status GNSS services, accessed Dec. 2020:

[1] https://www.gps.gov/systems/gps/space/

[2] https://glonass-iac.ru/en/GLONASS/

[3] https://www.gsc-europa.eu/system-service-status/constellation-information

[4] http://www.csno-tarc.cn/en/system/constellation

[5] https://sys.qzss.go.jp/dod/en/constellation.html

[6] https://www.isro.gov.in/spacecraft/list-of-navigation-satellites

where A is the amplitude, f the linear frequency, the period T is the time required to complete a cycle, and the circular frequency (angular velocity) ω.

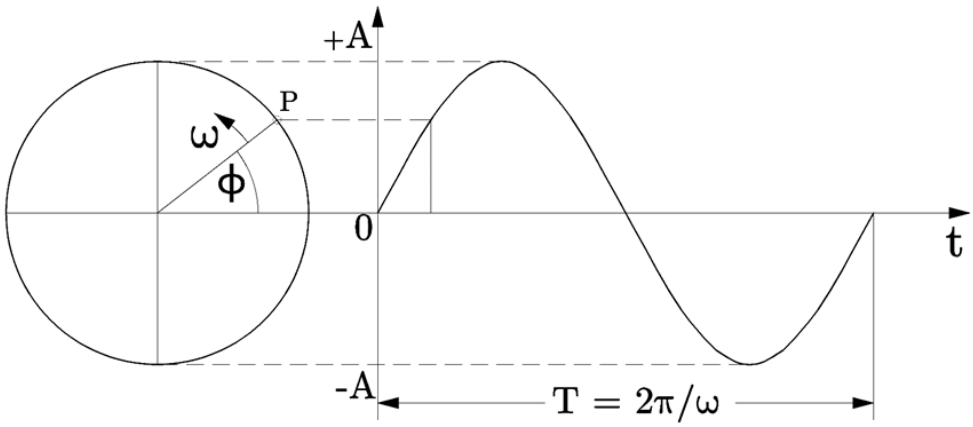

Figure 2.1. Phase representation of a sinusoidal wave. The point P rotates along the circumference with angular velocity ω. The P state in the instant t is defined by the phase ϕ given by $\phi = \omega t$. (based on [Hofmann-Wellenhof et al., 2008]

GPS relies on electromagnetic (EM) waves in which the electric field $\boldsymbol{E}$ and the magnetic field $\boldsymbol{B}$ oscillate sinusoidally. EM characteristics are described by Maxwell's equations which specify that a spatially varying electric field is associate with a magnetic field that changes over time. The harmonic representation of the electric and magnetic fields is given as follows

$$\boldsymbol{E}(x,t) = E_0 \cos\left(\frac{2\pi t}{T} - \frac{2\pi x}{\lambda} + \phi\right)\hat{\boldsymbol{e}} \tag{2.3}$$

$$\boldsymbol{B}(x,t) = B_0 \cos\left(\frac{2\pi t}{T} - \frac{2\pi x}{\lambda} + \phi\right)\hat{\boldsymbol{b}} \tag{2.4}$$

Where E_0 and B_0 represent the amplitude of the electric and magnetic field, respectively. The wavelength λ is the distance between identical points or contiguous crests in the adjacent cycles of the EM waves propagated in space.
The unit vectors $\hat{\boldsymbol{e}}$ and $\hat{\boldsymbol{b}}$ specify the direction that the electric and magnetic field oscillates. For an electromagnetic wave propagating through free space the

electric and magnetic fields oscillate perpendicular to the direction of propagation. Likewise, $\boldsymbol{E}$ and $\boldsymbol{B}$ oscillate perpendicular to one another. Variations in the direction of the electric field oscillations cause changes in its polarization, a property applying to EM waves described in the following subsection.

Electromagnetic Polarization

The electric field of an EM wave oscillates perpendicularly to the direction of propagation. The electric field can be expressed by the vector $\boldsymbol{E} = [E_x, E_y]$ which determines the polarization of the EM wave. If the direction of $\boldsymbol{E}$ is constant, then the EM wave has linear polarization. If exists a variation ratio between the elements of the vector $\boldsymbol{E}$, it reveals a circular or elliptical polarization. The rotation of $\boldsymbol{E}$ clockwise signifies a Right-Handed Circular Polarization (RHCP), counterclockwise indicates Left-Handed Circular Polarization (LHCP). When a linear polarized EM wave travels through ionized gases occurs a change in its polarization becoming circularly or elliptically polarized, an effect knows as Faraday rotation [Hofmann-Wellenhof et al., 2008]. Figure 2.2 shows a representation of vertical and horizontal linear polarization and how the changing direction of the electric field causes its circular polarization.

To reduce this effect, GPS signals are transmitted as Right-Handed Circular Polarized (RHCP). When the signal bounces off Earth's surface, depending on the reflecting surface properties and the incident/elevation angle of the transmitter and considering specular reflection, the reflected signal might change from RHCP to Left-Hand Circular Polarized (LHCP). Polarization observations can be used in GNSS-R applications. Hoseini et al., [2020], found an improvement of sea surface roughness estimation combining polarimetric observations from RHCP and LHCP signals determining also how the combination of RHCP and LHCP observations can improve the sensitivity of GNSS-R measurements to the change of sea state.

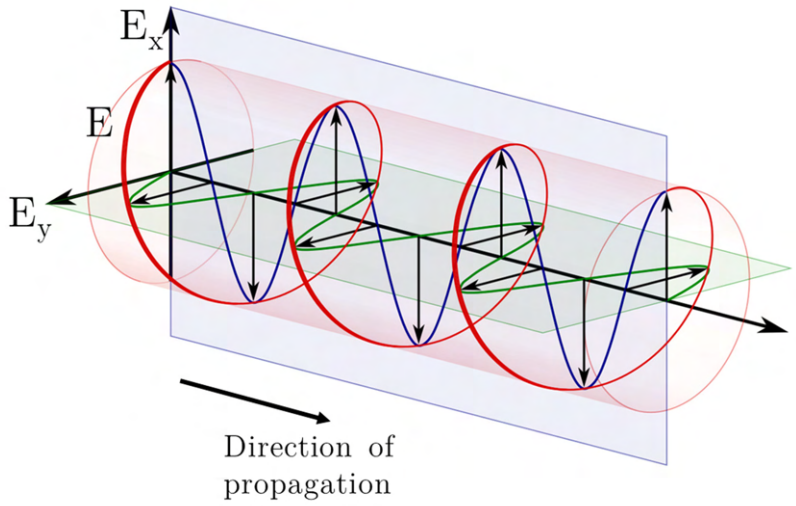

Figure 2.2. Linear and circular polarization. Linear vertical polarization (blue), linear horizontal polarization (green), and Right-Handed Circular Polarization (red). (based on ["Circular Polarization" 2020])

2.1.2 GPS Signal Structure

GPS satellites transmit signals that are based or derived from the generation of a fundamental frequency $f_0 = 10.23\ MHz$ [Hofmann-Wellenhof et al., 2001]. Two carrier signals in the L-band, denoted L1 and L2, are generated by integer multiplications of f_0 (integer multiplier are 154 and 120, respectively). The resulting frequencies have values of 1,575.42 Mhz and 1,227.6 Mhz. On these carrier frequencies, two types of codes are transmitted. The civil signal on L1 know as coarse/acquisition (C/A) code and the military signal on L1 and L2 is called the precision code (P).

Each satellite transmits a unique pseudorandom noise (PRN) code that serves as the satellite identifier (satellites in this thesis are identified by the number of PRN) and as a ranging code (determination of signal travel time from the satellite to the receiver). Besides, a navigation message is transmitted at a rate of 50 Hz. The message provides information about satellite ephemeris (Keplerian elements or satellite position and velocity), almanac, clock bias parameters, and satellite health status [Sanz Subirana et al., 2011]. The PRN code and the

navigation message are modulated together in the carrier frequency using a binary phase-shift keying (BPSK) scheme. Figure 2.3. shows a representation of how L1 and L2 signals are composed.

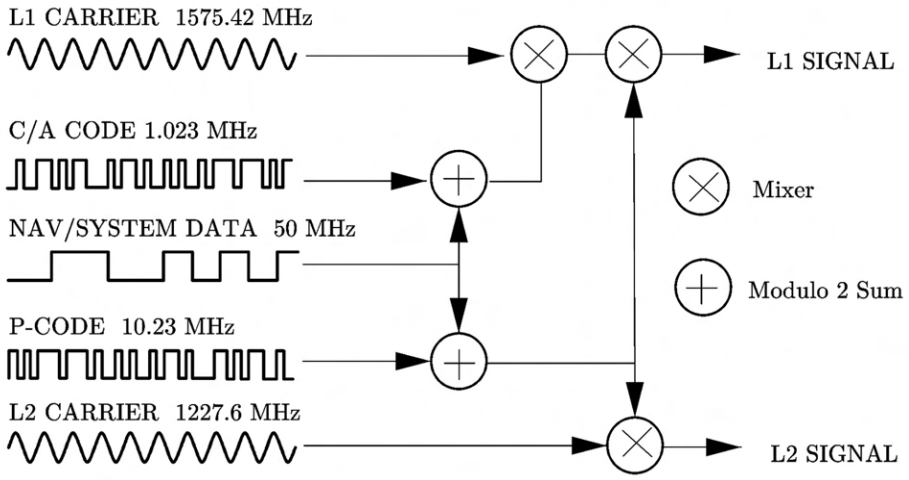

Figure 2.3. L1 and L2 GPS signal structure. (based on [Dana, 1998]).

GPS modernization has introduced additional carrier frequencies and codes, respectively, that will not be addressed in this document and that can be found in GPS books e.g., [Xu & Xu, 2016]

2.1.3 Signal Acquisition and Tracking

Signal Acquisition

According to [Ziedan, 2006] the acquisition step consists of a two-dimensional search process. The goal of the acquisition is to detect the signal coming from the visible satellites and the coarse estimation of C/A code delay (τ), and the Doppler frequency shift (f) caused by the motion of the satellites and/or the receivers. The two-dimensional search is represented in Figure 2.4. with the axis divided into suitable sections called bins which establish the delay and frequency resolution. To carry out the searching, the receiver generates a local replica C/A code of each satellite and correlates it with the received signal at all possible code delays and Doppler shifts (each combination of delay/frequency is represented in Figure 2.4 as a Delay-Frequency cell). By comparing the code delay

between the local code and the received code and the searched Doppler bin with the received Doppler, the correlation analysis can be formed. The maximum correlation is detected once the difference between the replica signal and the received signal becomes minimal.

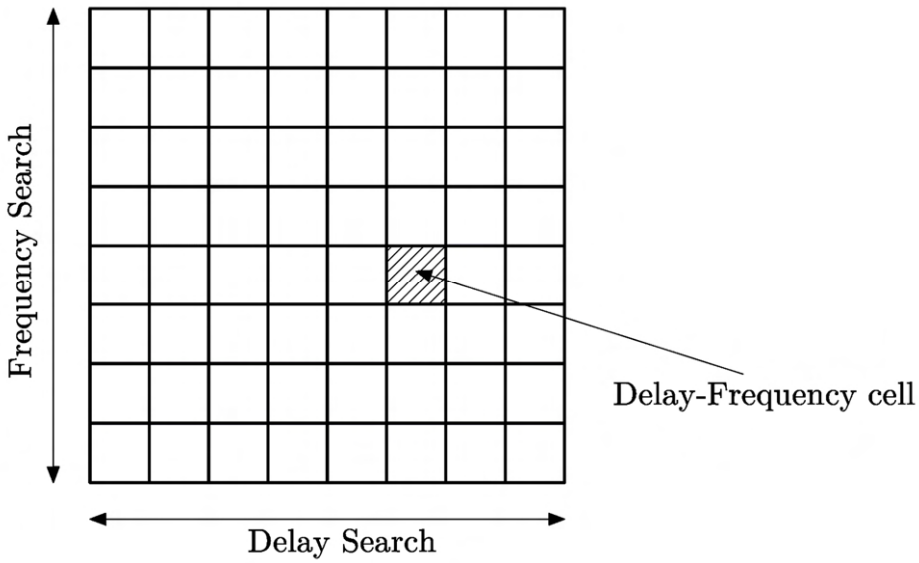

Figure 2.4: Delay and frequency acquisition search. Each domain is distributed in bins to search. The combination of delay and frequency form a cell.

The PRN code acquired, the coarse code delay, and Doppler shift in the acquisition step, allows us to initialize the tracking step.

Signal Tracking

In the tracking step, a refinement of the parameters obtained in the acquisition stage is carried out. The signal tracking allows us the estimation of refined delay τ, Doppler shift f, and the carrier phase ϕ. These refined parameters are extracted by using lock-loop synchronization architectures that can be configured in different strategies [Bacci et al., 2012]. The most common signal tracking module configuration comprises three iterative estimators for the parameters described above.

The carrier phase-locked loop (PLL) for carrier phase tracking responsible to maintain as close to zero as possible the phase error between the local replica and the incoming (acquired) signal considering the noise and interferences. The Frequency-locked loop (FLL) for carrier frequency tracking (using the coarse f obtained in the acquisition). The FLL serves to initialize the PLL. The latter will refine the frequency estimation employing a narrower bandwidth provided by the FLL which gives a frequency close to the correct one. Finally, the Delay-locked loop (DLL) for code delay tracking to obtain the refined delay from which the enhanced range between the satellite and the receive can be computed considering the bias introduced due to the very stable oscillators aboard the satellites in comparison with the local clock at the receiver.

2.2 GNSS Reflectometry

Global Navigation Satellite Systems has shown excellent performance in applications such as geodesy and geophysics, transportation, timing, defense, meteorology, and many other areas. In the last two decades, GNSS has gained an important role as a remote sensing tool. By analyzing the observed signals, applications such as atmospheric sounding and space weather can be realized. Most of these applications rely on the signals that directly reach the receivers. However, there is a portion of the signals that bounce off the Earth surface before they reach the receiver from which properties of the reflecting surface can be derived from the GNSS-R technique. This section presents the concepts of this technique and models and methods employed in obtaining results.

2.2.1 Observation Geometry

GNSS-R relies on the so-called geometry of the bistatic RADAR system, a system that uses antennas at different locations for transmission and reception [IEEE Standard, 2016]. In GNSS-R, the transmitter is the GNSS Satellite and the receiver is the antenna placed on a platform. The components and geometry that make up a GNSS-R system are shown in Figure 2.5 and described below.

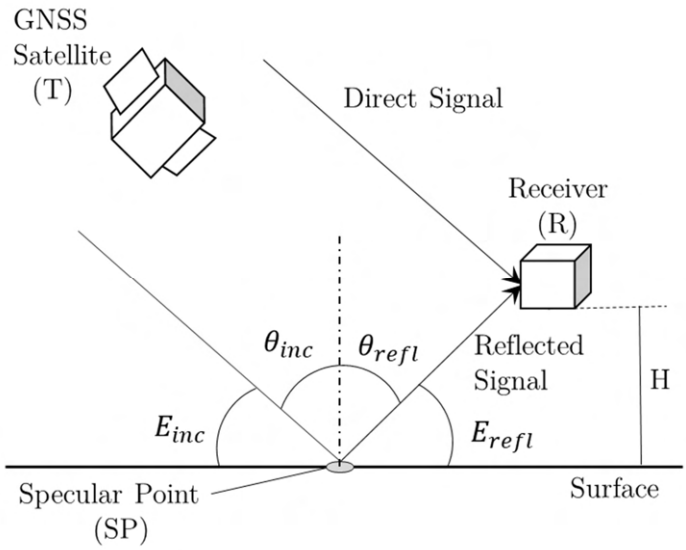

Figure 2.5: GNSS Reflectometry geometry representation, detailed description of the components is presented below.

- GNSS Satellite (Transmitter): Satellite that is part of one of the global satellite navigation systems, currently 130+ available.
- Direct signal: Signals that are captured directly by the GNSS-R receiver. These signals maintain their polarization as they were broadcasted by the GNSS satellite, that is, Right Hand Circularly Polarized (RHCP).
- Reflected signal: Signals that are captured by the receiver once they have been reflected off Earth's surface. They might change their polarization to Left Hand Circularly Polarized (LHCP).
- GNSS-R receiver (Platform): It is the platform on which the antenna that will receive direct and reflected signals is installed, there are different types of platforms: LEO Satellites, aircraft (airplane, zeppelin, gyrocopter), ships, or ground stations.
- Reiver height (H): The height of the receiver measured with respect to the reflecting surface.
- Elevation (E) and Incident (θ) angles: E is the angle of the reflected signal with respect to the surface. θ is the complementary angle of the E.

- Specular point: It is the point that minimizes the Transmitter-Surface-Receiver distance and where the elevation angle E between the direct and the reflected signal with respect to the surface normal, are equal.

2.2.2 Reflection Process

The reflection of an electromagnetic wave is a complex process that is primarily influenced by the dielectric properties of the surface such as conductivity and permittivity and its geometric structure given by the roughness [Darrozes et al., 2016]. Specular reflection occurs when a wave transmitted with specific power is reflected in one direction with a loss of power due to the absorption of the reflecting surface. On the other hand, in diffuse reflection, the wave is scattered in multiple directions and the power is dispersed through these directions. Figure 2.6 illustrates a representation of specular and diffuse scattering which is mainly determined by the roughness parameter σ_s of the surface.

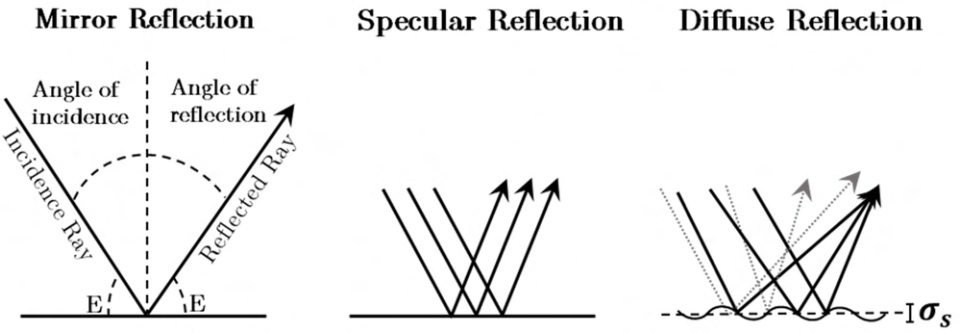

Figure 2.6: Representation of specular and diffuse reflection. The parameter σ_s serves to define the surface roughness, typically represented by the standard deviation of the mean level of surface variations.

The incoherent reflection component dominates as the surface roughness increases. A common criterion to considerate a smooth surface depending on the wavelength and elevation angles is given by the “Rayleigh criterion” that reads

$$\sigma_s < \frac{\lambda}{8 \sin E} \tag{2.5}$$

Where σ_s is the standard deviation of the mean level of the surface, λ the wavelength of the L-Band, and E the elevation angle. If a maximum phase difference of $\pi/4$ or $\pi/8$ between all the scatters that contribute to the scattering process is expected, the factor 8 in eq. (2.5) needs to be changed by 16 or 32, respectively.

GNSS-R Reflectivity Modeling

The analysis of the observed power of reflected and direct signal, represented by the sea state factor (subsequently related to sea state parameters) is defined by the construction and analysis of the O–C (observed minus computed) approach. The computed part (C) is obtained by the model established in [Nievinski & Larson, 2014], which extends the model proposed in [Zavorotny & Voronovich, 2000] and [Zavorotny et al., 2010]. The power modeling of the direct and reflected signal considers the broadcasted signal (direct and reflected signals path, elevation/incidence angle, polarization), receiver height, random surface roughness, surface properties, antenna gain pattern, and antenna orientation. The modeled power of the direct (superscript D) and reflected (superscript R) signals, considering right hard circular polarization (subscript r), are simplified as

$$P^D = P_r^D G_r^D (W^D)^2 \tag{2.6}$$

$$P^R = P_r^D |XSW^R|^2 \tag{2.7}$$

The direct signal power model involves the component P_r^D that corresponds to the direct signal power collected by the antenna/receiver. The antenna gain, G_r^D which describes the efficiency of the antenna when it converts the radio waves coming from multiple directions and satellites into electrical power. The correction of this antenna gain pattern component has been disregarded in this study. W^D is the called Woodward ambiguity function incorporated as a result of the correlation process between the received signal and the local replica. The ambiguity function can be approximated by the autocorrelation function Λ, dependent on the delay difference, and the normalized sinc function (Fourier Transform) Γ, dependent on the frequency difference, as $W \approx \Lambda\Gamma$.

On the other hand, the reflected signal power model includes the reflection coefficient X derived from the solution of the Fresnel equations that involve the incident angle and the dielectric properties of the surface (permittivity and conductivity). The random surface roughness S characterizes the loss of coherent power calculated based on [Beckmann & Spizzichino, 1987] as

$$S = \exp(-0.5k^2\sigma_s^2 \cos^2\theta) \tag{2.8}$$

Where $k = 2\pi/\lambda$, the parameter σ_s is the standard deviation of the mean level of surface variations, and θ the incidence angle.

Finally, from the modeled power of the direct and reflected signal, the computed reflectivity can be calculated as

$$R_c = \frac{P^R}{P^D} \tag{2.9}$$

Delay Doppler Map

As presented in section 2.1.3 the GNSS signal detection is done by a cross-correlation process with local replicas. In the waveform, this correlation is seen as a peak "triangular" shape at the reception delay, representing power above the noise level when the maximum correlation is found, i.e., the signal and replica contain the same code modulation. A secondary peak can be identified when specularly reflected signals reach the receiver. So, they will produce a similar waveform to the direct signal but at a longer delay due to an extra travel path as it bounces off the Earth's surface. The reflected signal has contributions of both coherent and incoherent reflections therefore the signal spreads in Delay and Doppler frequency. A detailed explanation about the obtention of the delay and Doppler frequency shift in the correlation process can be found in Darrozes et al., [2016] and Jin et al., [2014]. The representation of the waveform in specular and diffuse reflection at different surface conditions is shown in Figure 2.7.

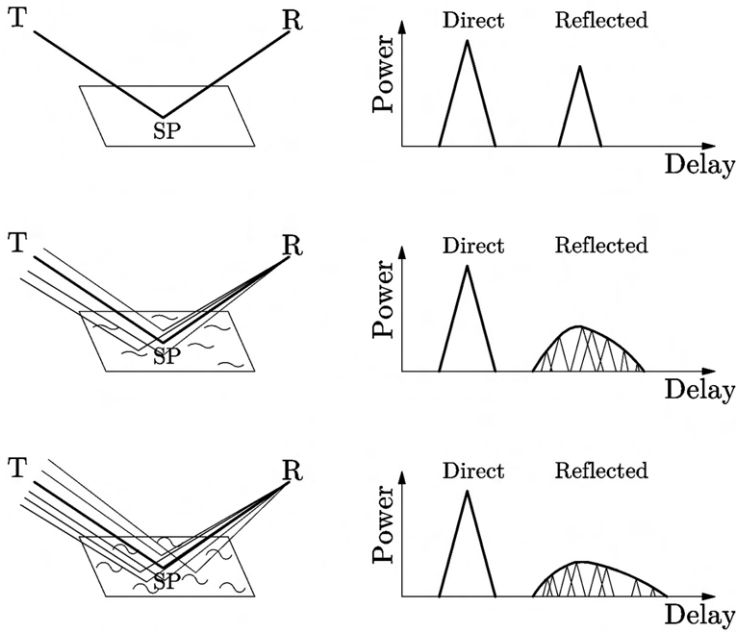

Figure 2.7: Direct and reflected signal waveform representation. **(top)** purely specular reflection zero roughness. **(middle)** Reflection on low roughness surface (calm sea state). **(bottom)** Reflection on high roughness surface (high sea state). T is the transmitter (GNSS satellite), R the receiver, and SP the specular point.

A notable power loss of the reflected signal is found as the sea surface roughness increases, the asymmetry of the waveform is attributed to the individual low and far from the specular point contributions. The fundamental observable that shows the power variations versus the delay and Doppler shift is the Delay Doppler Map (DDM). It reveals the contributions of the different delays and Doppler pairs from the different locations of the reflecting surface. The DDM can be used to estimate reflecting surface parameters e.g. height surface and roughness characterization, (see [Park et al., 2016] and [Marchan et al., 2008]) by using the path delay for ocean altimetry and the reflected power for roughness estimation (sea state.). An example of the DDM retrieved in this study is presented in Figure 2.8. There is evidence of reflection events by the occurrence of the second peak with a longer code delay [chips].

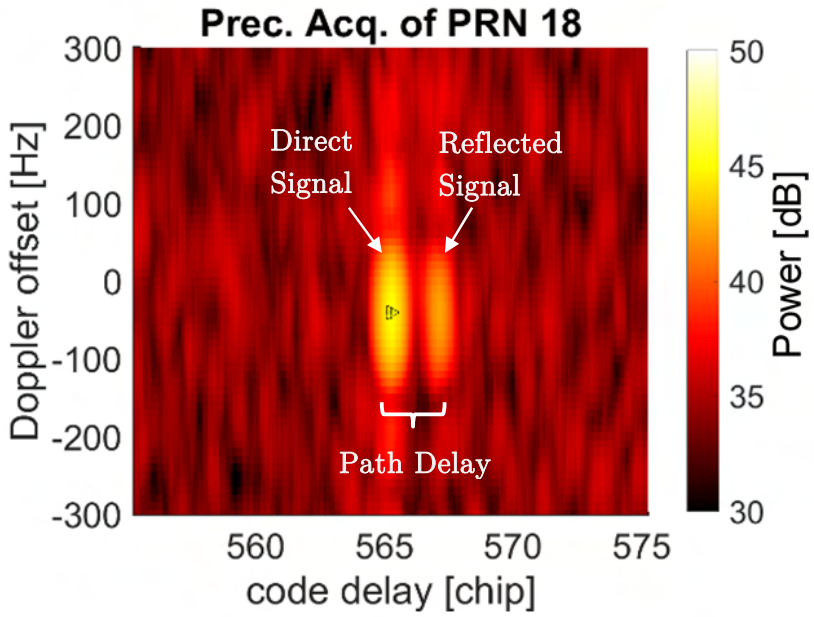

Figure 2.8: Delay Doppler Map for the airborne experiment. PRN 18 on 2019-07-17.

2.2.3 Interferometric Approach

The interferometric approach relies on the superimposition of electromagnetic waves that causes a phenomenon of interference from which is possible to retrieve information. The software receiver allowed us to track the carrier of direct signal and obtain interferometric observation of the reflected signal by detecting the difference between both signals. The interferometric approach described in the following is based on [Kucwaj et al., 2017] and [Semmling et al., 2011].

Direct Signal Tracking

The civil GPS L1 signal (direct) received from the satellites at instant t described in Kucwaj et al., [2017] is given by

$$S^D = A^D CA\left(t - \tau^D(t)\right)\sin(2\pi f^D t - \phi^D) + \eta^D(t) \tag{2.10}$$

Where A^D is the amplitude of the direct signal, CA is the CDMA in the coarse/acquisition signal broadcasted by the satellite and η^D is the Gaussian

noise with zero mean, f^D the Doppler frequency, τ^D the code delay, and ϕ^D phase delay.

In the acquisition step, coarse code delay and Doppler shift are obtained. Assisted by these parameters the tracking step follows. Tracking of the direct signal is done by using conventional GPS tracking loops. A general description of tracking loops can be found in the literature (e.g. [Ziedan, 2006] or [Bacci et al., 2012]). As presented in section 2.1.3, the three main types of tracking loops utilized in GPS are: Delay lock loop (DLL), phase lock loop (PLL), and Frequency lock loop (FLL) from which the refined parameters f^D, τ^D, and ϕ^D are retrieved. By using these parameters local replicas of the direct signal can be constructed.

The sine wave S^D can be expressed as the sum of sine and cosine functions. The sine part is called the in-phase component (I) and the cosine part is called quadrature (Q) [Scharf & Schreier, 2010]). The local replica represented as in-phase I_0^D and quadrature Q_0^D components is then written

$$I_0^D = CA\ (t\ -\ \tau^D)\ \sin(2\pi f^D t - \phi^D(t)) \tag{2.11}$$

$$Q_0^D = CA\ (t\ -\ \tau^D)\ \cos(2\pi f^D t - \phi^D(t)) \tag{2.12}$$

Reflected Signal Tracking

The GPS L1 reflected signal received from the satellites after bouncing off the Earth surface at instant t described in Kucwaj et al., [2017] is given by

$$S^R = A^R CA\ (t - \tau^D(t) - \Delta_{\mathrm{p}}(t)/c)\sin(2\pi f^D t - \phi^D - \psi(t)) + \eta^R(t) \tag{2.13}$$

Where A^R is the amplitude of the reflected signal, c is the speed of light, η^D is the Gaussian noise with zero mean, Δ_{p} is the path difference (see section 2.2.4) between the direct and reflected signal and ψ is the phase difference between the direct and reflected signal.

The reflected signal is tracked by using a Delay open-loop tracking (DOL). The latter is aided by the external model that provides the reflected delay $\tau^R = \Delta_p / c$. The local replica of the direct signal is used to demodulate the reflected signal at the instant k separated by the coherent integration time T_c of $20ms$ (same used in the direct signal tracking) as follows

$$I_0^R = \int_{k\ T_c}^{(k+1)\ T_c} S^R(t) I_0^D(t) dt \tag{2.14}$$

$$Q_0^R = \int_{k\ T_c}^{(k+1)\ T_c} S^R(t) Q_0^D(t) dt \tag{2.15}$$

The interferometric in-phase and quadrature observations can be defined modeled then as:

$$I_0^R = \frac{A^R}{2}\ \Lambda\ (\Delta_{\mathrm{p}}\ /\ c) \cos(-\psi)\ +\ \eta^I \tag{2.16}$$

$$Q_0^R = \frac{A^R}{2}\ \Lambda\ (\Delta_{\mathrm{p}}\ /\ c) \sin(-\psi)\ +\ \eta^Q \tag{2.17}$$

In-phase and quadrature components then only depend on the amplitude of the reflected signal and the modeled path difference. They also contain the phase difference ψ between the direct and reflected signal. The autocorrelation function of the CDMA code is Λ.

The raw data was sampled at 16.368 MHz. The direct and reflected I_0 and Q_0 components are normalized by a factor of data sampling multiplied by the integration time T_c ($20ms$). Removal of data bits the reflected in-phase and quadrature components are corrected (denoted by subscript c) by using the sign function of the direct in-phase component I_0^D as follows

$$D = \text{sign } I_0^D, \tag{2.18}$$
$$I_c^R = I_0^R D,$$
$$Q_c^R = Q_0^R D$$

Later, a low pass filter is applied to filter the low frequencies and reduce the noise.

Different signal processing applications use complex signal representation since they facilitate many mathematical manipulations (see [Scharf & Schreier, 2010]). The complex representation of the reflected filtered signal will be given by its phasor denoted as $\gamma_c^R = I_c^R + iQ_c^R$

Signal Re-tracking

The general aim of this step is to retrieve the phasor residual γ from γ_c^R and a phasor built from the model path difference Δ_p. From the latter, the modeled phase difference is obtained in eq. (2.19) where λ is the wavelength of the GPS L1 signal (~$0.1904m$).

$$\psi_p = \text{mod}[2\pi \ \Delta_p/\lambda \ , 2\pi] \tag{2.19}$$

The phasor in complex representation reads

$$\gamma_p = \exp[-i\psi_p] \tag{2.20}$$

Finally, the residual phasor γ is derived from

$$\gamma = \gamma_c^R \gamma_p^* \tag{2.21}$$

Where * denotes the complex conjugate of the modeled phasor. In the following, γ is called the interferometric phasor and the in-phase and quadrant representation is $\gamma = I + iQ$ (super- and subscripts removed)

2.2.4 Signal Path Model

To determine the interferometric observation, it is necessary to establish the path of propagation of the direct and reflected signal to model the specular point position and the path difference Δ_p. The latter is used in the open-loop for the reflected signal tracking and as presented in section 2.2.3. Based on Semmling et al., [2012] the signal path can be modeled with an aided Earth-curvature model refined by a complex ray-tracing model for altimetric precise results. The ray-tracing model includes the correction of refractivity effects on the signal when it is passing through the troposphere and ionosphere. The tropospheric refractivity is modeled by using the temperature, pressure, and humidity parameters, and the ionospheric refractivity by the distribution of electron density in the assumed time-invariants F- and E-layers. These effects are neglected in this study.

This study is focused on sea roughness, therefore the signal path modeling by the aided Earth-curvature approach is sufficient. This model employs an approximated specular point based on a priori receiver height H on a simple planar surface geometry, represented in Figure 2.5, which serves as input to retrieve a more precise specular point position considering the Earth's curvature. To include the Earth's curvature in the specular point position an osculation sphere can be defined at the proximity of the planar-approximated specular point position that locally fits the curvature of the ellipsoid WGS-84. The planar approximated and true specular points are assumed to be close, so it is possible to make the relation between the osculation sphere radius and the ellipsoidal height of the reflecting surface. Figure 2.9 shows a representation of the a priori planar signal path model and Figure 2.10 the Earth-curvature model. Distances and angles have been exaggerated to distinguish the differences.

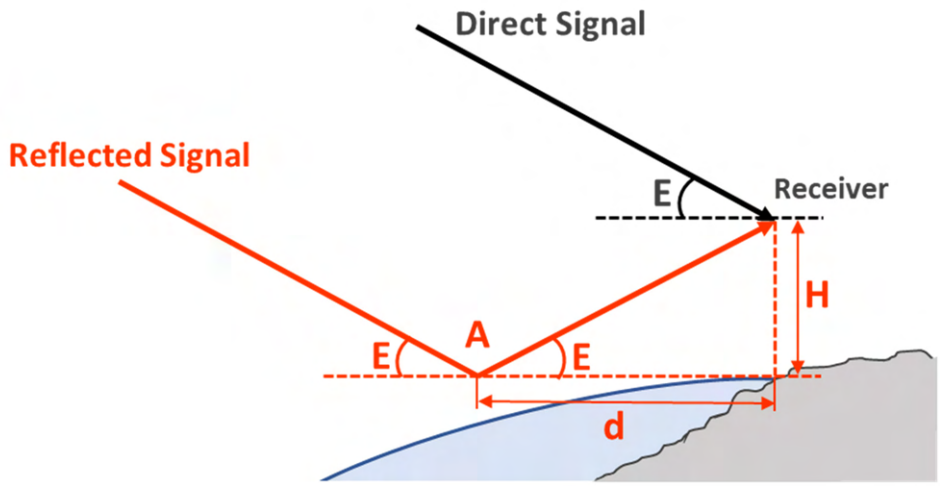

Figure 2.9: Planar model representation. Angles $E - E$ are equal in specular reflection and the same as the angle formed between the horizontal plane and the direct signal. Distance d is the distance from the receiver to the approximated specular point and H is the approximated heigh of the receiver.

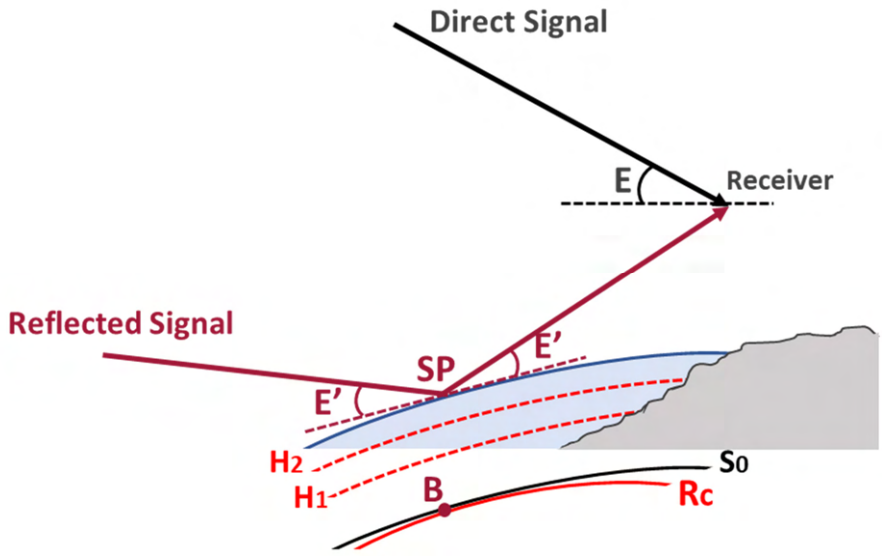

Figure 2.10: Earth curvature model representation. When the Earth curvature is considered, the angle E' differs from the satellite elevation angle E at the receiver location. B is the projection of the approximated specular point A and the point where the ellipsoid surface S_0 and osculation sphere R_c meet. From it, different height H_j are set until the surface heigh is reach and the true specular point SP is located.

From topocentric receiver coordinates, the azimuth and elevation of the transmitter in the receiver position are estimated. The a priori height H is calculated by using the ellipsoidal height (h) of the receiver and the height of the Geoid above the ellipsoid (N) at the specific location. The latter is called Geoid undulation. Considering the Geoid as the idealized continuation of the mean surface of the ocean (under the influence of the gravity and rotation of Earth alone) receiver height is then $H = h - N$. The estimation of N is provided by the geoid model, in this case, the EGM-96 model. With H and E parameters, the distance d is derived by

$$d = \frac{H}{\tan E}$$

And the estimation of the path difference can be computed from

$$\Delta_p = 2H \sin E$$

From d and E in the planar approximation, it is possible to derive spherical coordinates of point A which will be then refined by the Earth-curvature model retrieving the true coordinate of the specular point SP and therefore the corrected path difference. A detailed description of the algorithm can be found in Semmling et al., [2012].

2.3 Sea State Parameters - Ancillary Data

Ancillary data was obtained from the ECMWF ERA5 model. The ERA5 is the fifth-generation reanalysis for the global climate and weather for the past 4 to 7 decades. ERA5 offers public-use data hourly estimates of many atmospheric, land, and oceanic climate variables from 1979 to within 5 days of real-time. The updated reanalyzes provide a numerical description of the recent climate by combining models at finer spatial and temporal resolutions.[7]

[7] https://www.ecmwf.int/en/forecasts/datasets/reanalysis-datasets/era5

Wind speed and Direction

ERA5 model provides wind data in raster format ($GRIB$) represented by eastward and northward wind vectors called u and v components respectively (see Figure 2.11) from which wind speed and direction can be derived. $\boldsymbol{\phi}$ is the angle of the direction from which the wind is blowing and the magnitude of $\vec{V}$ is the wind speed.

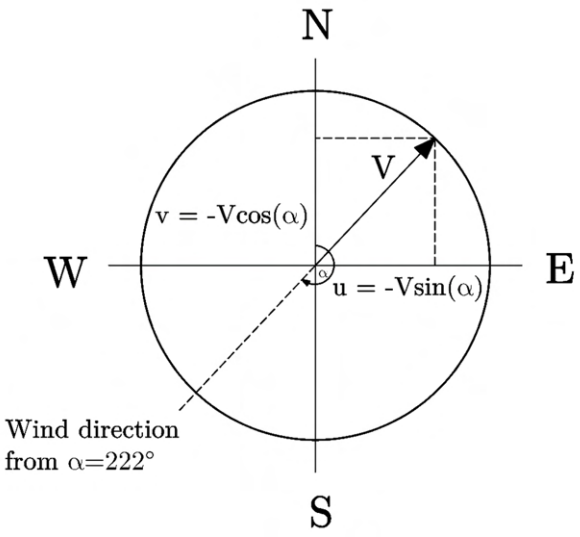

Figure 2.11: Wind components representation

Whit $u = -|\vec{V}| \sin\alpha$ and $v = -|\vec{V}| \cos\alpha$ wind speed is given by

$$|\vec{V}| = \sqrt{u^2 + v^2}$$

And the wind direction is obtained from

$$\alpha[deg] = 180° + \frac{180°}{\pi} \text{atan2}(v, u)$$

The function atan2 considers the sign of both arguments to determine the quadrant.

The wind parameters used for computation from ERA5 are the “10m u-component of wind” and “10m v-component of wind” which are the horizontal speed

of air moving towards the east and north, at a height of ten meters above the surface of the Earth in meters per second[8].

The results are two raster files (*GeoTIFF*) with 18km of spatial resolution that contains pixel values of the wind speed and wind direction, respectively. These files were retrieved for each date of data collection.

Significant Height Wave

ERA5 model provides different parameters for height waves in raster format (*GRIB*). The "significant height of combined wind waves and swell" is used in this study. This parameter represents the average height of the highest third of surface ocean/sea waves generated by wind and swell used for coastal applications[9]. Formally, it is the vertical distance between the wave crest and the wave trough in meters as represented in Figure 2.12.

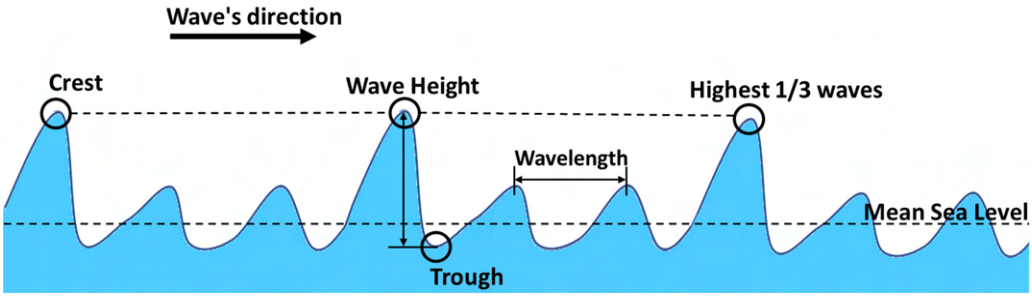

Figure 2.12: Significant height wave. It denotes the characteristic height of the random waves in a sea state.

The SWH data from ERA5 has some pixel without information along the north-south segment analyzed. A raster extrapolation is performed to fill the missing information of SWH. The result is a raster file (*GeoTIFF*) with 25km of spatial resolution that contains the significant wave height information in all the pixels that overlap with the flight trajectory.

[8] https://cds.climate.copernicus.eu/cdsapp#!/dataset/reanalysis-era5-single-levels?tab=overview
[9] https://cds.climate.copernicus.eu/cdsapp#!/dataset/reanalysis-era5-single-levels?tab=overview

3 Flight Experiment and Data Analysis

This section introduces information about the flight experiment. Besides details about the study area, the antenna setup, used platform, and flights, and captured data information can be found. The first analysis based on the DDM is performed to establish the reflection events and determine the trajectory section of higher reflection response.

3.1 Study Area Description

The flights were performed in the coastal area between Calais and Boulogne, which have ~50 km along the coastline, see the map in Figure 3.1.

Figure 3.1: Experiment location and the flight trajectory from Calais to Boulogne-sue-Mer coast in the North Sea, English Channel.

During measurements dates the wind speed was between ~2.5m/s to ~6.5m/s in the flight area (ancillary data obtained from ERA5 model, see section 2.3). Figure 3.2 shows variations of wind speed and direction in 4 days of the measurements campaign. On 2019-07-17 is the date with lower wind speed and SWH, that is lower sea state.

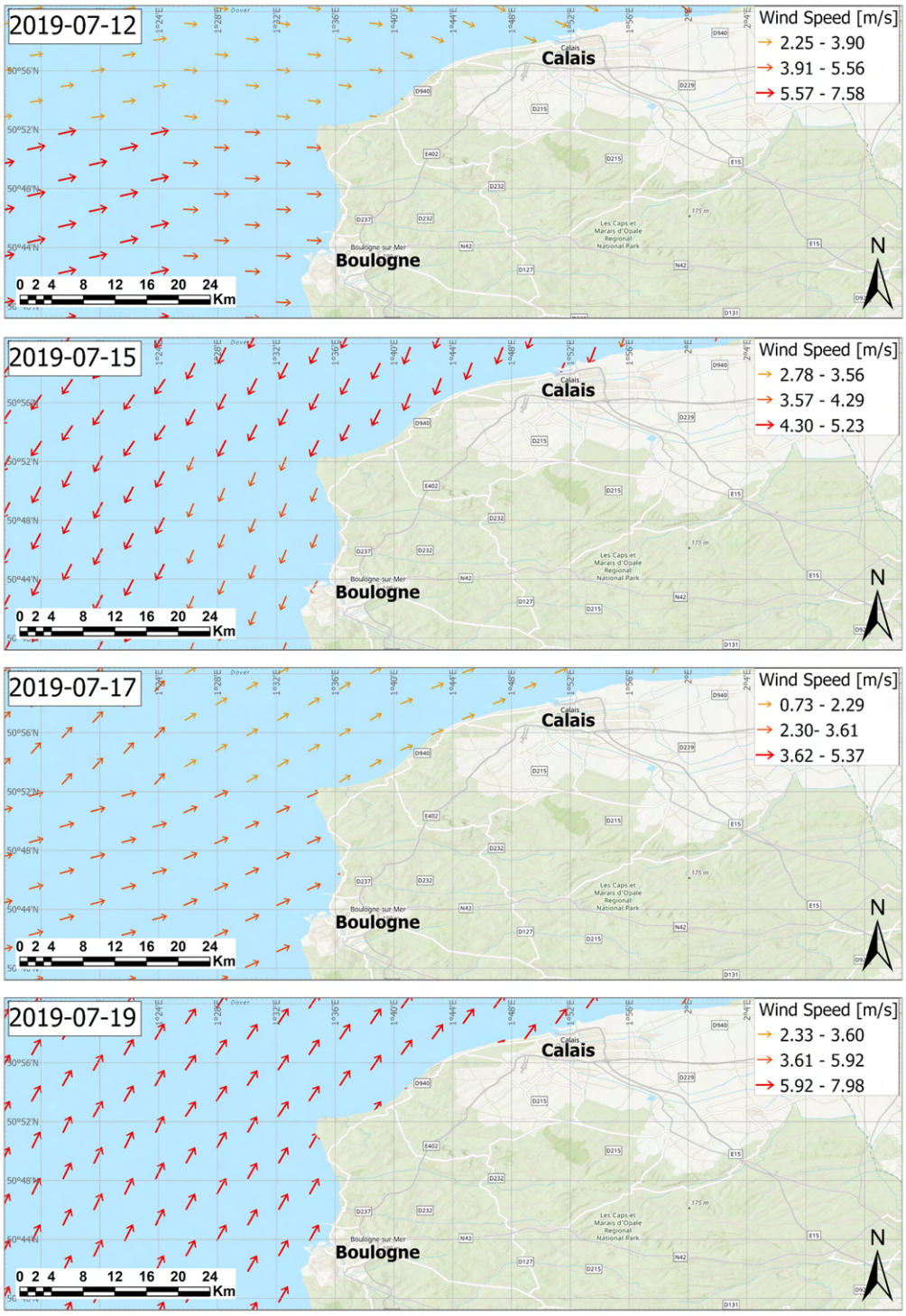

Figure 3.2: Wind speed and direction variations in the study area from ERA5 Model lower sea state on 2019-07-17 and higher on 2019-07-19.

Wind speed and direction, and SWH on the study area are shown in Table 3.1. The flights on the 12th, 15th, 17th, and 19th are selected for the analysis in this thesis as will be explained in section 3.4.1.

Date	Wind speed [m/s]	Wind direction [deg]	SWH [m]
2019-07-09	2.30	112	0.22
2019-07-11	3.78	235	0.28
2019-07-12	5.49	117	0.30
2019-07-15	4.29	67	0.58
2019-07-17	2.92	204	0.26
2019-07-19	6.50	240	0.55

Table 3.1: Sea state parameters during the measurements campaign

3.2 Platform and Antenna Set-up

The platform used is a gyrocopter (see Figure 3.3). As being a microlight aircraft driven by autorotation it can fly extremely slowly while being very agile. This aircraft can be flown safely and steadily under both strong wind and turbulent conditions. The aim of this study in terms of the platform is to evaluate the functionality of the gyrocopter as a platform for GNSS - R coastal monitoring.

Figure 3.3: Aircraft used in the experiment. (1) GNSS - R antenna, (2) Extra GPS antenna + INS for flight control purposes.

A dual-polarization antenna (with right- and left-handed circular polarization) was used for the GNSS-R measurement. The antenna was in the front of the aircraft tilted ~43° with respect to the zenith direction. In GNSS -R experiments it is common to use an arrangement of antennas, generally single polarized (RHCP) antenna up-looking and single polarized (LHCP) antenna down or side-looking, both linked to a common receiver in a Master-Slave configuration aligning the direct and reflected signal and creating the correlation depending on the baseline between both antennas. The dual-polarized antenna used in the experiment permitted to capture of the direct and reflected signal at a baseline equals to zero, and transmit the signals captured through 2 dedicated links towards two independent front-end receivers, one for RHCP signals and the other for LHCP signals. The aim of this study in terms of antenna setup is to evaluate the functionality of a custom dual-polarized antenna, and 2 different receivers storing the data independently to synchronize and process the signal records with a software receiver afterward. Figure 3.4 illustrates the aircraft frame with zoom in the antenna configuration.

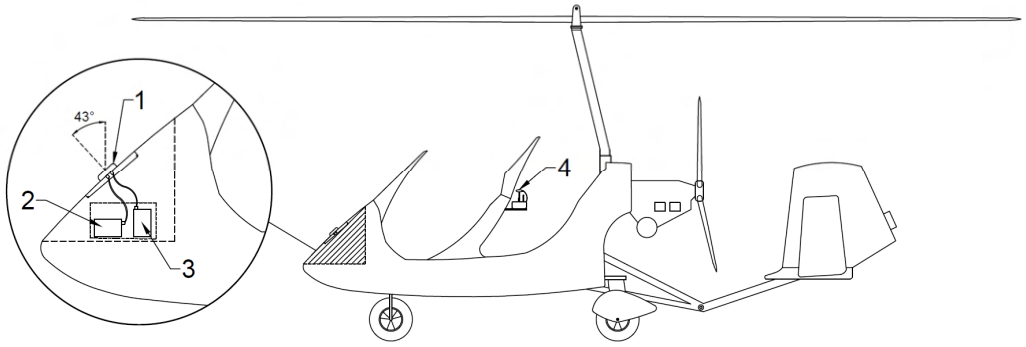

Figure 3.4: Antenna set up on board of aircraft. (1) Dual polarized antenna, (2) Receiver for RHCP signal, (3) Receiver for LHCP signal, (4). Extra GPS+INS flight control.

3.3 Flight Information and Data Sets

Airborne GNSS - R covers large areas, however, they are limited in time. Thanks to the versatility in different wind conditions, it was possible to perform flights with similar trajectories along the coast on multiple days. This enables us to obtain multitemporal data at different hours each day. Variable sea state conditions can be expected depending on wind speed, daytime, the hour of the day, weather, and tides conditions. The flight design will be assessed based on the results obtained. Table 3.2 presents an overview of flight information.

	Description
Flight days	09, 11, 12, 15, 17, 19 July 2019
Altitude	~750 m.a.s.l
Avg. Speed	50 km/h
Flight duration	~2h
Total Flight time	13h 40m

Table 3.2: Fights information

The detailed timeline of flights is presented in Figure 3.5.

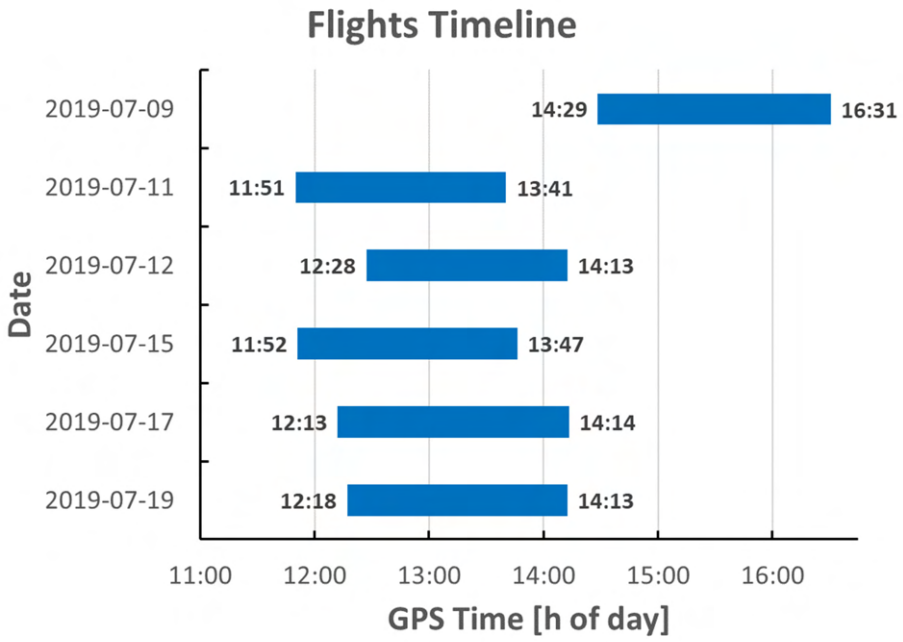

Figure 3.5: Flights timeline in the measurements campaign. Flights were conducted during similar GPS time except on 2019-07-09.

Flight design consisted of two legs (one forth, one back) in the distance from the coastline, of 700 m and 2 km, respectively. The average covered distance per flight was 120 km, ~55 km each leg + distances from Calais airport to the coast. Figure 3.6 presents the flight trajectories performed each flight day.

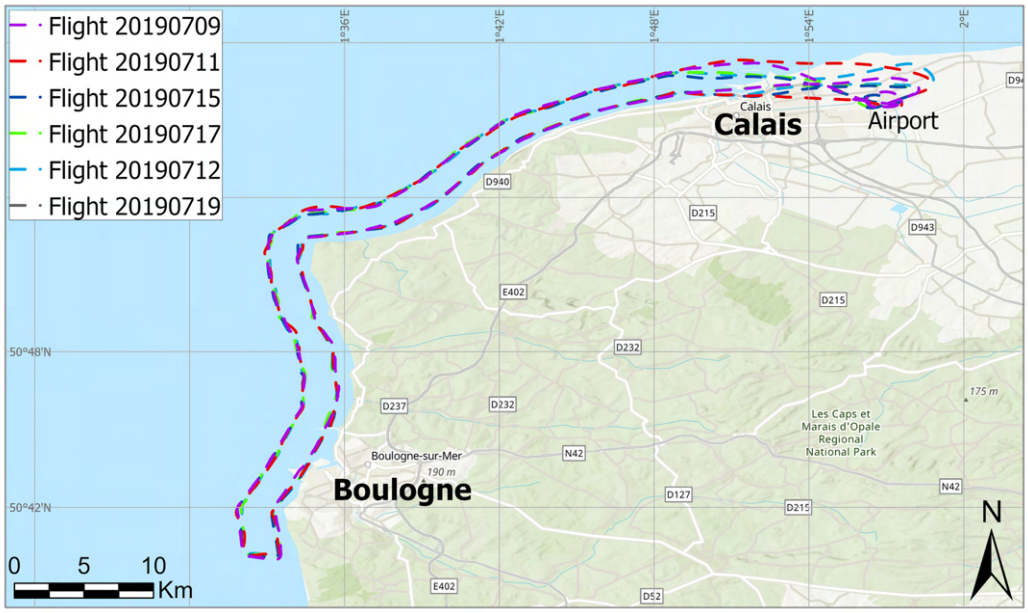

Figure 3.6: Flight trajectories between Calais and Boulogne during the measurements campaign. The starting and ending point is the Calais airport.

Due to the total flight time (13h 40m), a large amount of data could be collected, which gather a total of 139.09 GB. Six flights were conducted, two flights provided data sets for RHCP and LHCP signals, two flights provided single data set for RHCP signals, and one flight provided data only for LHCP signals. Table 3.3 shows a summary of the data collected and its distribution.

N	Date	RHCP		LHCP	
		Data Size [GB]	Duration [min]	Data Size [GB]	Duration [min]
1	2019-07-09	14.64	122	0.00	0
2	2019-07-11	0.00	0	13.94	116
3	2019-07-12	12.64	105	12.61	105
4	2019-07-15	13.80	115	0.00	0
5	2019-07-17	14.56	121	14.56	121
6	2019-07-19	13.80	115	0.00	0
	TOTALS	**84.19**	**702**	**54.90**	**458**

Table 3.3: Data organization and the total amount of data.

3.4 Data Analysis and Processing

The preliminary analysis consisted of determining the best data set to obtain consistent results when estimating the observation of the sea state that allows the comparison between distinct WS and SWH during the measurements campaign. From

3.4.1 Reflection Events Analysis

From the DDM, it is possible to assess the evolution of the reflection events through platform trajectory for each day of data collected. The evaluation is made for the RHCP and LHCP signals. Initially, DDMs every 900 seconds are retrieved from which the total reflection events are obtained (see Figure 3.7). The results show that RHCP signals pose a higher number of reflection events, so the analysis is focused on these.

The days selected for the assessment are 2019-07-12, 2019-07-15, 2019-07-17, and 2019-07-19 due to wind speed and wind direction varied conditions and similar flight period (from ~12:00 to ~14:00).

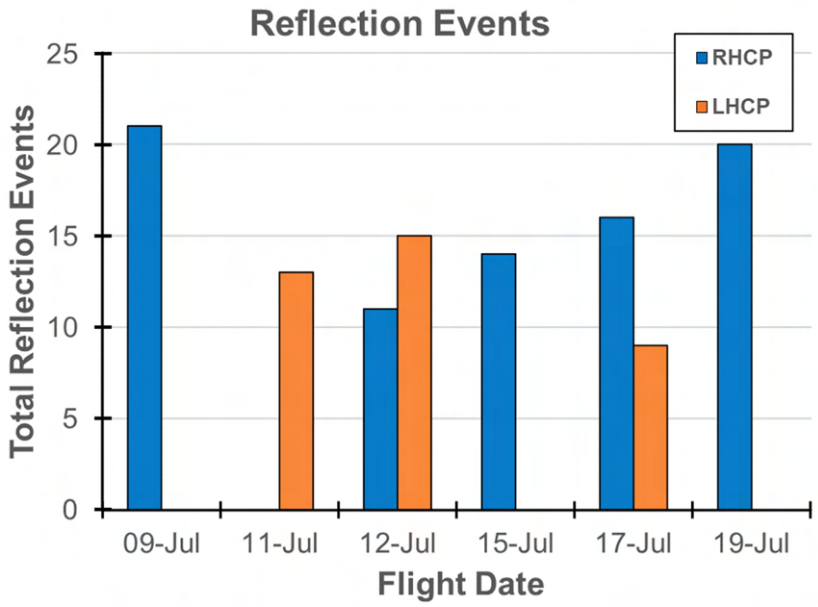

Figure 3.7: Total reflection events from 2019-07-09 to 2019-07-19 computed from Delay Doppler Map every 900 seconds.

A complimentary evaluation is presented in Figure 3.8 that shows the reflection events occurrence with the satellite's elevation evolution through measurements time.

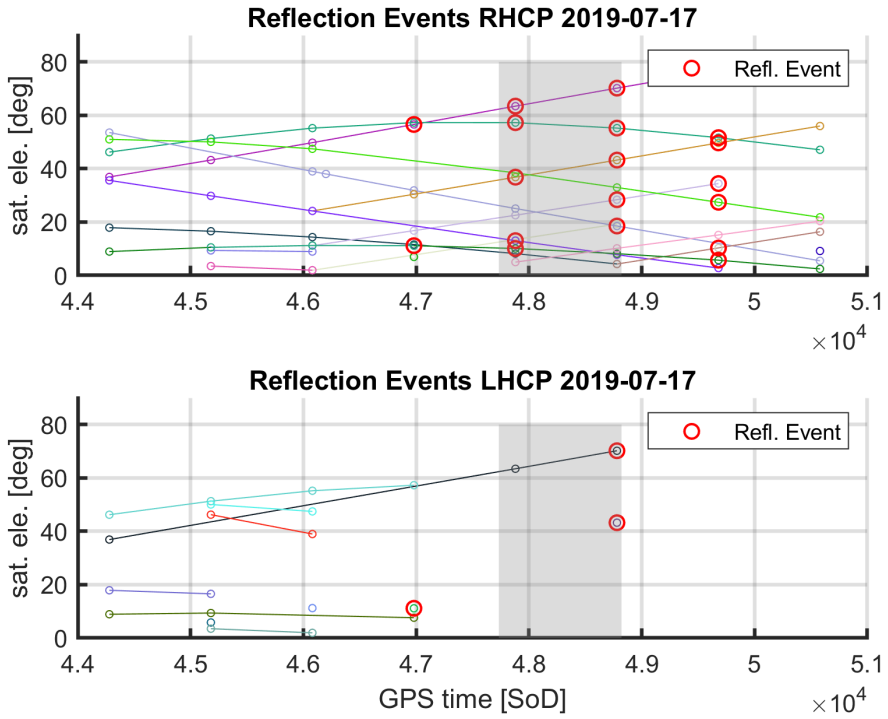

Figure 3.8: Reflections events along tracked satellite elevation. The shaded segment represents the time interval of the best reflection response. It can be seen reduced tracked satellites and reflection events from the LHCP signal.

The analysis reveals that the second of the day (SoD) GPS time from 47733 to 48753 on 2019-07-17 has the best reflection response (this interval can vary depending on flight date, see Table 3.4). This period falls on the north-south segment of the gyrocopter trajectory that begins at the place known as Cap Gris Nez (see Figure 3.9). Once this segment is passed, different satellite signals are lost due to the big change in sight angle and because of the gyrocopter body blocking the signals.

Date	SoD Start	SoD End	Duration [min]
2019-07-12	47828	48788	16
2019-07-15	45625	46465	14
2019-07-17	47733	48753	17
2019-07-19	47603	48803	20

Table 3.4: Starting and ending GPS time [SoD] of north-south segment trajectory on the selected days for analysis.

Figure 3.9: Flight trajectory 2019-07-17 tagged every 60s, in the north-south segment. This segment starts at the point known as Cap Gris Nez and finishes at Équihen-Plage

3.4.2 Data Processing

The general workflow of data processing is presented in this section (see Figure 3.10) including the components and retrievals for each data level established. Acquisition, tracking step, and DDM description have been already introduced in the theory and definitions section (subsections 2.1.3 and 2.2.2 respectively). Modeling, validation, and final retrievals are described in detail in section 0.

The RHCP and LHCP data was sensed in a dual-polarized antenna linked to two independent single front-end receivers. As described in reflection events analysis, this study is focused on the RHCP signals. A software receiver is implemented to track the direct and reflected signals by using locked- and open-loops, respectively. The observations of the reflected signal power and its Doppler distribution are retrieved to determine their correlation with the sea state ancillary data and evaluate the experimental configuration.

The data processing involved four data levels as follows:

- Analog Level: Radiofrequency GPS signals sensed by the dual-polarized antenna.
- Data Level (0): The raw data samples at a frequency of 16.368MHz provided by two independent single front-end receivers one for right-hand and one for left-hand circular polarized signals.
- Data Level (1): The Delay Doppler Map (DDM) from acquisition and tracking steps. First observable that allow determining reflection events and direct and reflected signal parameters for further processing and validation.
- Data Level (2): Sea state factor and Doppler Frequency Shift of the reflected signal every minute from interferometric observable obtained at a rate of 50 Hz.

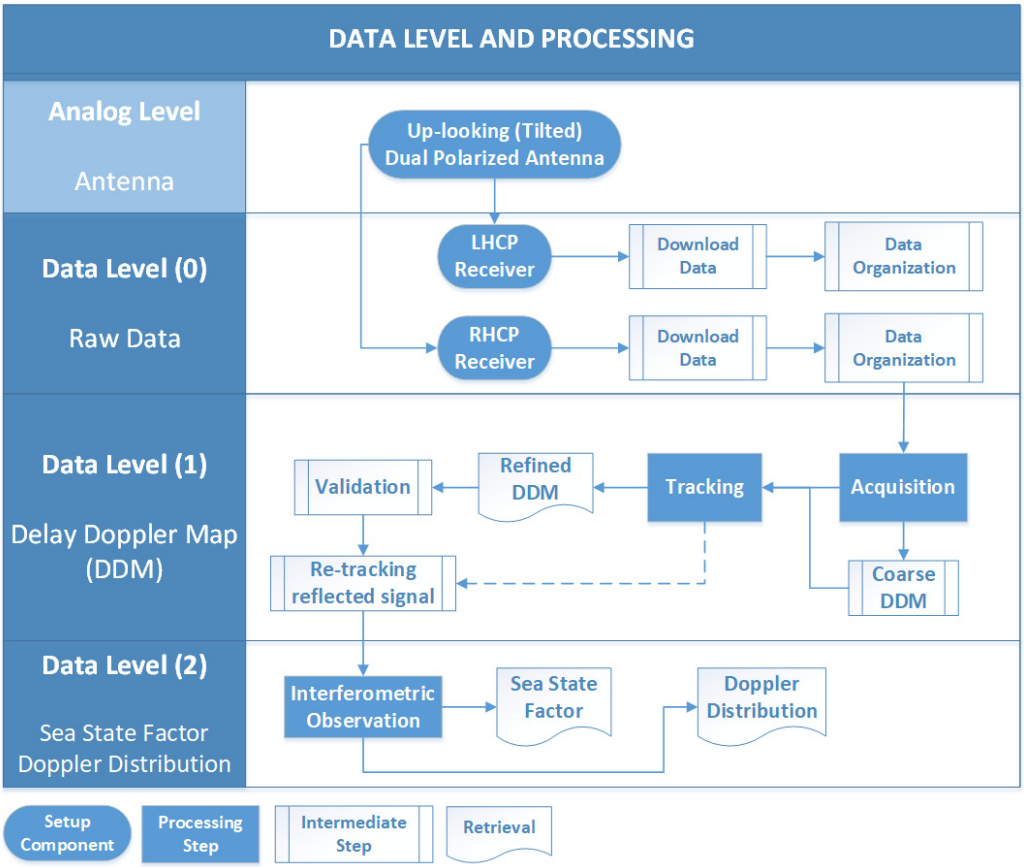

Figure 3.10: Scheme of data levels and general processing steps. Only right-hand circular polarized signals are processed in this study.

4 Modeling and Retrievals Results

This section presents the modeling of specular point position and the modeled path difference used in the aided open loop for the tracking and re-tracking of the reflected signal. Besides, it describes the validation step to determine the agreement between modeled path difference and the observed path difference computed from the Delay Doppler Maps. Furthermore, it presents the estimation of the observed direct and reflected signal power and the reflectivity and Doppler distribution from the power spectral density approach. Finally, it describes the correlation of the sea state factor and Doppler shift standard deviation with respect to ancillary sea state parameters (wind speed and significant wave height) obtained from the ECMWF ERA5 model.

4.1 Signal Path Modeling and Validation

A precise model of signal path propagation is fundamental to obtain consistent interferometric observations. Although the tropospheric and ionospheric corrections are neglected for this study, the path difference from the Earth-curvature model showed a great agreement with the path difference retrieved from the code delay found in the DDM obtained from the acquisition and tracking steps. The modeling of the path difference and the validation against the observed path difference are presented below.

4.1.1 Specular point position

The position of the GNSS satellite (transmitter) and receiver are required to determine the modeled specular point position as described in section 2.2.4. Broadcasted ephemerides are used to calculate the position of the transmitter. The position of the receiver is calculated in the absolute (stand-alone) positioning method. From the topocentric receiver coordinates, the azimuth and elevation of the transmitter in the receiver position are derived. Figure 4.1 presents the sky plot with a total of 15 visible GPS satellites at the point near Cap Gris Nez at 13:15, this number of visible satellites variates over time. From azimuth and elevation of the GPS satellite, and coordinates and height of the receiver, the computation of the specular points for each visible PRN along the platform trajectory is performed.

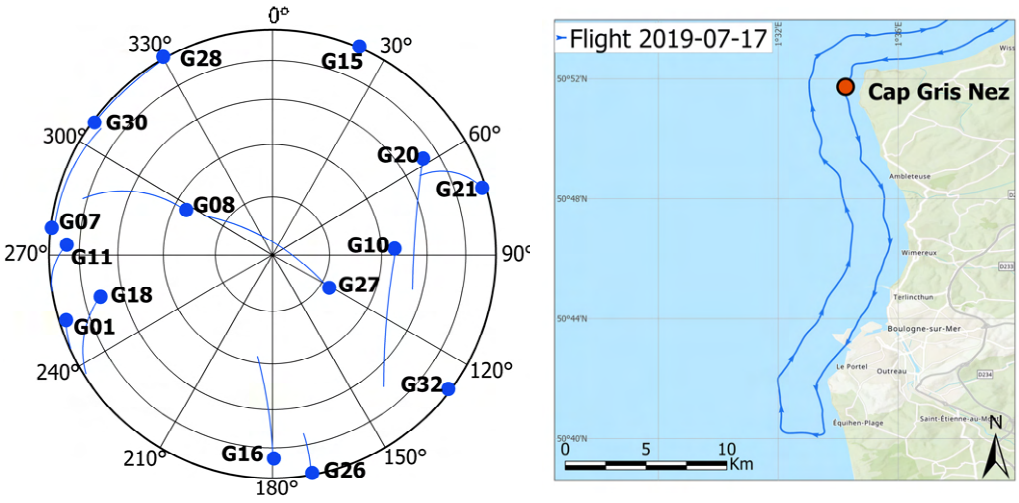

Figure 4.1: Sky plot of the visible events on 2019-07-17 at 13:15 in Cap Gris Nez **(left)**. Location of starting north-south segment, Cap Gris Nez **(right)**.

The retrieved tracks of the modeled specular points locations are shown in Figure 4.2. Most of the events located in the east of the segment analyzed projected their respective specular points position on the land surface. The traces over land could be used to detect soil moisture from airborne GNSS-R measurements. However, all land reflections are excluded since the focus of this study is to determine the sensitivity in the properties of the sea surface.

From the visible satellites, a selection of a subset is done based on the following conditions: ensure adequate distribution in azimuth and different elevation angles to analyze different events locations, and successfully tracked satellites from which the specular point position lies strictly on the ocean surface. The final satellites selected for this study are PRN 1, 7, 8, 10, 11, 16, 18, 27, 30. However, not all the reflection points of these satellites are located on the sea surface. Some of them fall in the vicinity of the beach. To avoid these locations of reflection points, a land mask is defined. The masking process excludes all points located on the ground and points that are located up to 250 meters from the official coastline. The latter condition is defined to avoid points where the reflectivity response can be influenced by the areas where the sea waters and the ground converge.

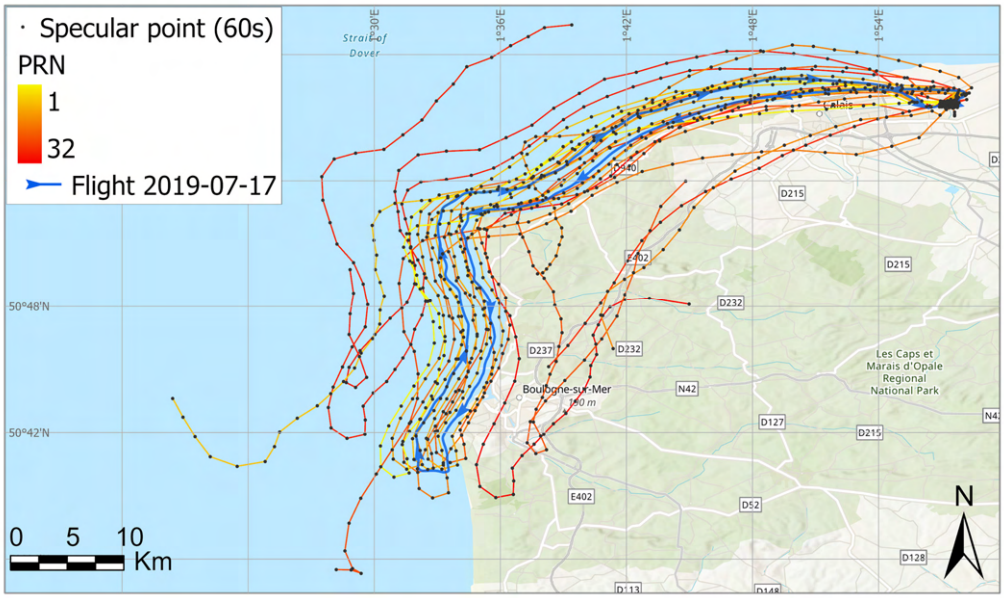

Figure 4.2: Specular points track and mark every 60s for visible satellites in the study area on 2019-07-17.

Figure 4.3 shows the specular points tracks of the selected events in the north-south trajectory segment with specular points every 60s.

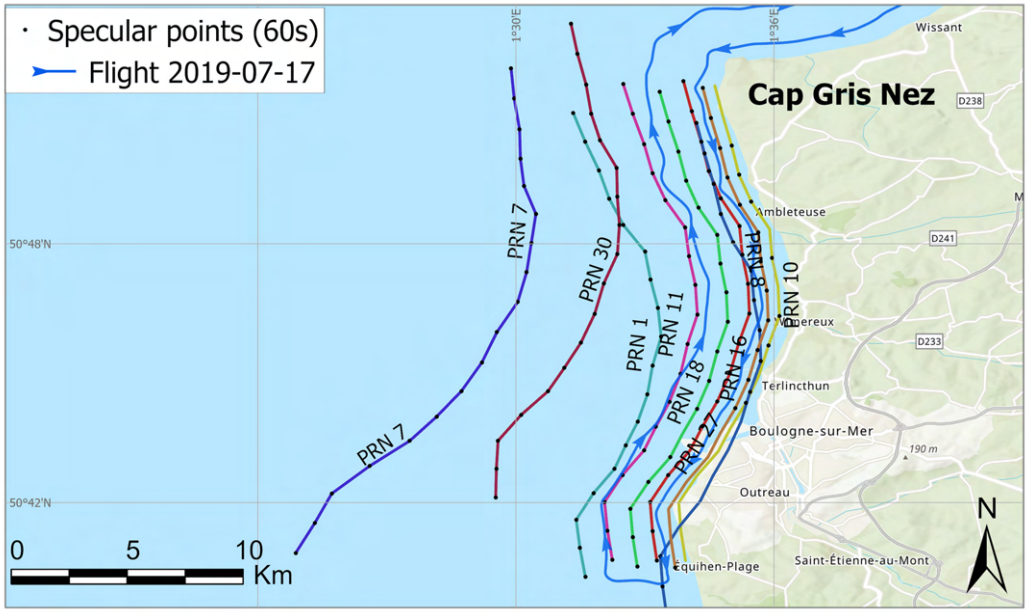

Figure 4.3: Selected events with specular points every 60s in the north-south segment trajectory.

4.1.2 Modeled Path Difference

The modeled path difference between the direct and the reflected signals is computed based on the GNSS-R signal path geometry described in section 2.2.4. To calculate the path difference Δ_p, the receiver height (H) and elevation (E) at the receiver position are required. H is estimated by using the ellipsoidal height (h) and the Geoid undulation (N). The ellipsoidal height of the receiver is retrieved from the absolute (stand-alone) positioning method and, the estimation of Geoid undulation is retrieved from the *EGM-96* geoid model. By using these two parameters, the height H at the specific location along the aircraft trajectory is estimated by using the relation $H = h - N$. Figure 4.4 shown the modeled path difference (in meters) variation of PRN 18 in the specular points track on 2019-07-17.

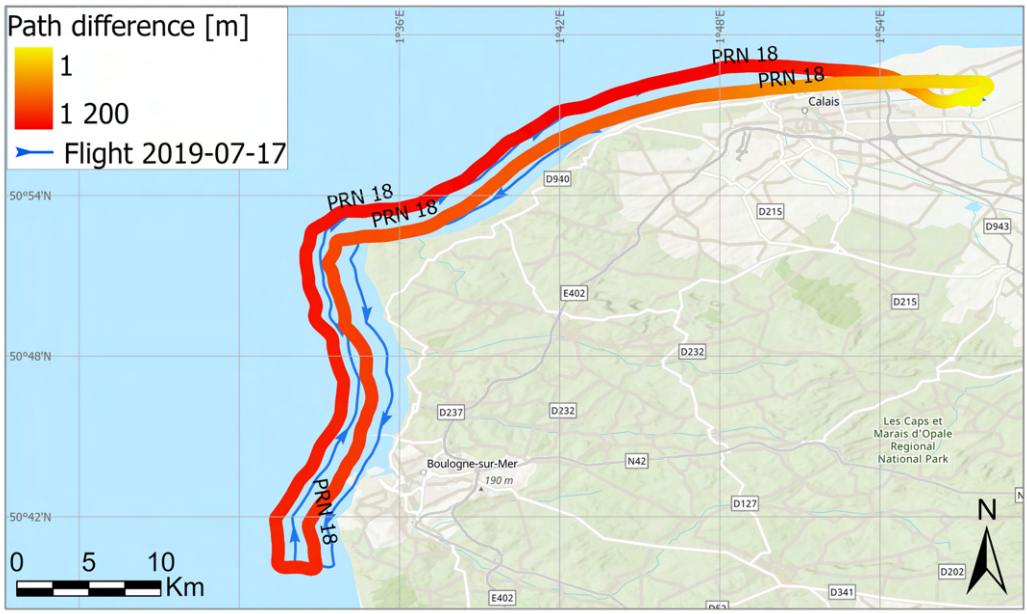

Figure 4.4: Modeled path difference Δ_p for PRN 18 (2019-07-17). The difference at take-off and landing instant (yellow section) is reduced due to the distance from the receiver to the surface is small.

As expected, the modeled path difference computed from the transmitter's azimuth and elevation and receiver's coordinates, considering the Earth's curvature, increases as the platform increases its height. The yellow section refers to the taking off and landing area in the Calais airport. Besides, the modeled path difference increases also at greater elevation angles as can be seen in Figure 4.5.

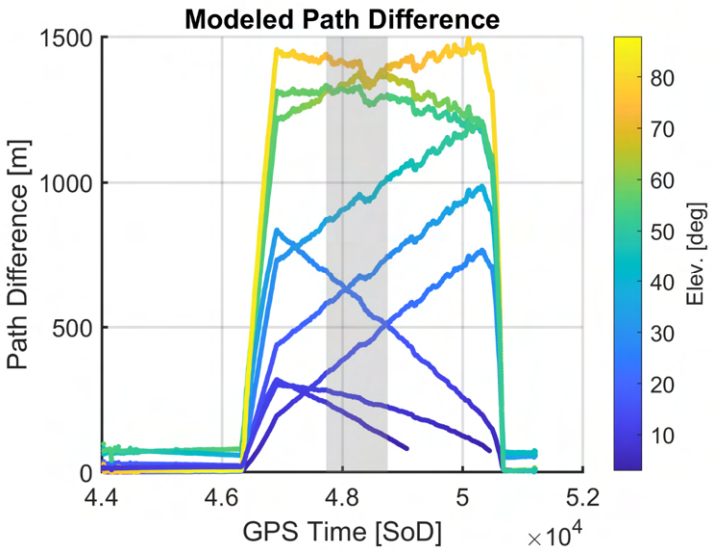

Figure 4.5: Modeled path difference at different elevation angles on 2019-07-17. north-south segment shaded in gray.

The modeled path difference increases or decreases rapidly at events with an elevation angle between 10° to 60°. At an elevation above 60°, these path difference variations are not as pronounced since the specular point tracks are located closer to the position of the receiver (flight trajectory).

Modeled Path Difference Validation

The validation step is done to evaluate the agreement between the specular modeled path difference and the path delay retrieved from DDM computation. In the acquisition step, initial values for code delay and Doppler shift are calculated. The tracking step uses the previous values to retrieve accurate estimates of the parameters code and phase delay and Doppler shift. Refined and accurate DDM are computed every minute to perform the validation.

Based on the DDM reflected peak the time interval of the best reflection response is established to concentrate the analysis along this period. For evolution representation, Figure 4.6 shows the DDM for PRN 18 on 2019-07-17 in the interval of GPS time, second of the day (SoD): 46980 (13:03:00) to 49980 (13:53:00) every 10 minutes.

During this period, the evolution of the reflected peak can be observed before entering the north-south segment of the platform trajectory and how it vanishes once the segment has passed.

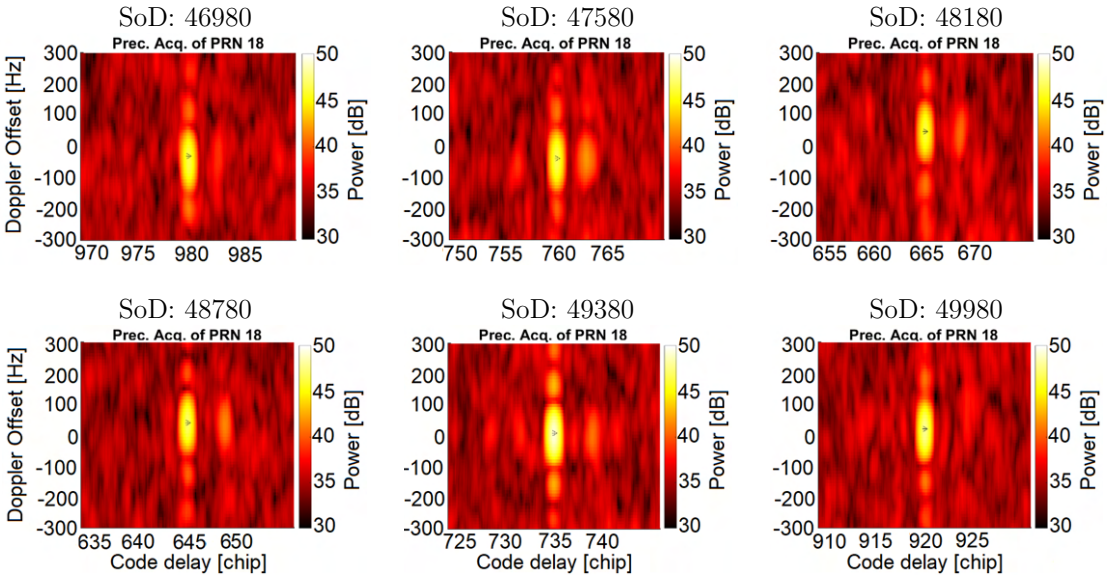

Figure 4.6: DDM on 2019-07-17 for PRN 18, in the interval [46980,49980] second of the day. The reflection response is identifiable approximately at 47580 and starts to vanish after the second of day 49380.

From the code delay of the reflected signal with respect to the direct signal peak in the DDM, the path difference can be computed in meters. There is an agreement between the DDM retrieved and modeled path difference as shown in Figure 4.7. This result shows an accurate definition of the signal path model. Although tropospheric and ionospheric effects are disregarded in this study, the Earth's curvature signal path model is precise enough to validate the DDM observations. Once this agreement is identified, it is possible to establish events with specular reflection from the captured data, therefore it is feasible to compute the correlation between the ancillary sea state parameters and the observables and determine the sensitivity degree.

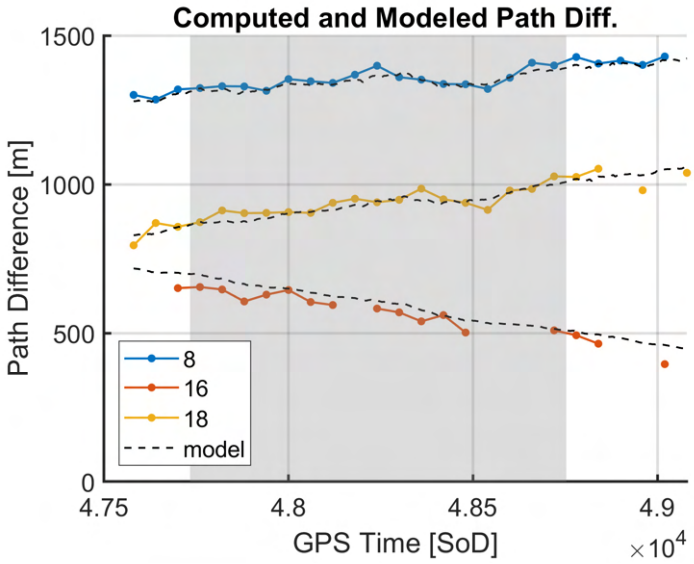

Figure 4.7: Path differences from DMM computation and specular modeled at high (PRN8), mid (PRN18), and low (PRN16) elevation events on 2019-07-17. North-south segment shaded in gray.

The DDMs in this validation step were retrieved every minute. Gaps in the path difference retrievals from DDM are caused because it was not possible to track the respective satellite during that interval.

4.2 Sea State Observation

4.2.1 Power Spectral Density

The interferometric phasor γ denoted in section 0 (reflected signal re-tracking) is represented in the time domain, however, the power presented in the frequency domain reveals more information about the reflected signal. This representation is usually in the form of a power spectral density (PSD). The PSD techniques have been investigated in different studies in GNSS-R, e.g. [Semmling et al., 2013; Semmling, M., 2012]. PSD represents the power distribution of the time signal into different frequencies. To obtain the PSD the Fast Fourier Transform (FFT) of a time signal can be applied, and the Inverse Fourier Transform (IFT) can be used to transform the frequency domain signal to the time domain signal [Lee, 2005]. The Fourier Transform Γ of the interferometric phasor γ is given by

$$\Gamma(v) = \int e^{-i2\pi vt}\gamma(t)dt \tag{4.1}$$

The Fourier Frequency v is considered for formal description. The Doppler frequency is used for the following analyses.

The PSD allows identifying the peaks and their respective Doppler frequency shift in the specific integration time. In the reflection process, the power retrieved of the reflected signal is related to the roughness of the surface and the geometry (elevation angle) configuration. The spectrum for each PRN presents a power peak. A sharp peak in the spectrum means specular reflection conditions, so a smooth surface is considered (low sea state), so the power of the reflected signal increases. For the spread spectrums, which describes a reduction of the power of the reflected signal, a rough surface is found thus a higher sea state.

Figure 4.9 and Figure 4.8 show the PSD (logarithmic scale) of the reflected signal in a frequency interval around zero on 2019-07-17 (WS: 2.92 $m/s, SHW$: ~0.26) and 2019-07-12 (WS: 5.49 $m/s, SHW$: ~0.30) respectively . The integration time is one minute, and the retrievals are located along the north-south segment selected. Columns in these figures, distinguish events at different elevation angle, low: $E < 10°$, mid: $10° < E < 30°$, and high: $E > 30°$. Each spectrum contains the reflected raw complex signal (blue), reflected signal after the low-pass filter (red), reflected re-tracked signal which rectifies the peak towards zero frequency and reduces the spread of the Doppler frequency shift (yellow), and the modeled path difference converted into frequency domain (black).

Sharper and defined peaks are identified at low sea state (2019-07-17) and low and mid-elevation angles which presents consistency between the power of the observed reflected signal and the modeled. As the elevation angle increases, the incoherent component begins to dominate the reflection process, so spread spectrums are obtained and there is no evidence of defined peaks that excel to the noise level that allows defining a specular reflection. The broadening in the spectrum also depends on the roughness of the sea surface. On 2019-07-12 (higher sea state), the spectrums are more spread out than those on 2019-07-17. So, incoherent reflection is obtained due to the contribution in the reflection process from multiple scatters in a different direction due to due to increased surface roughness.

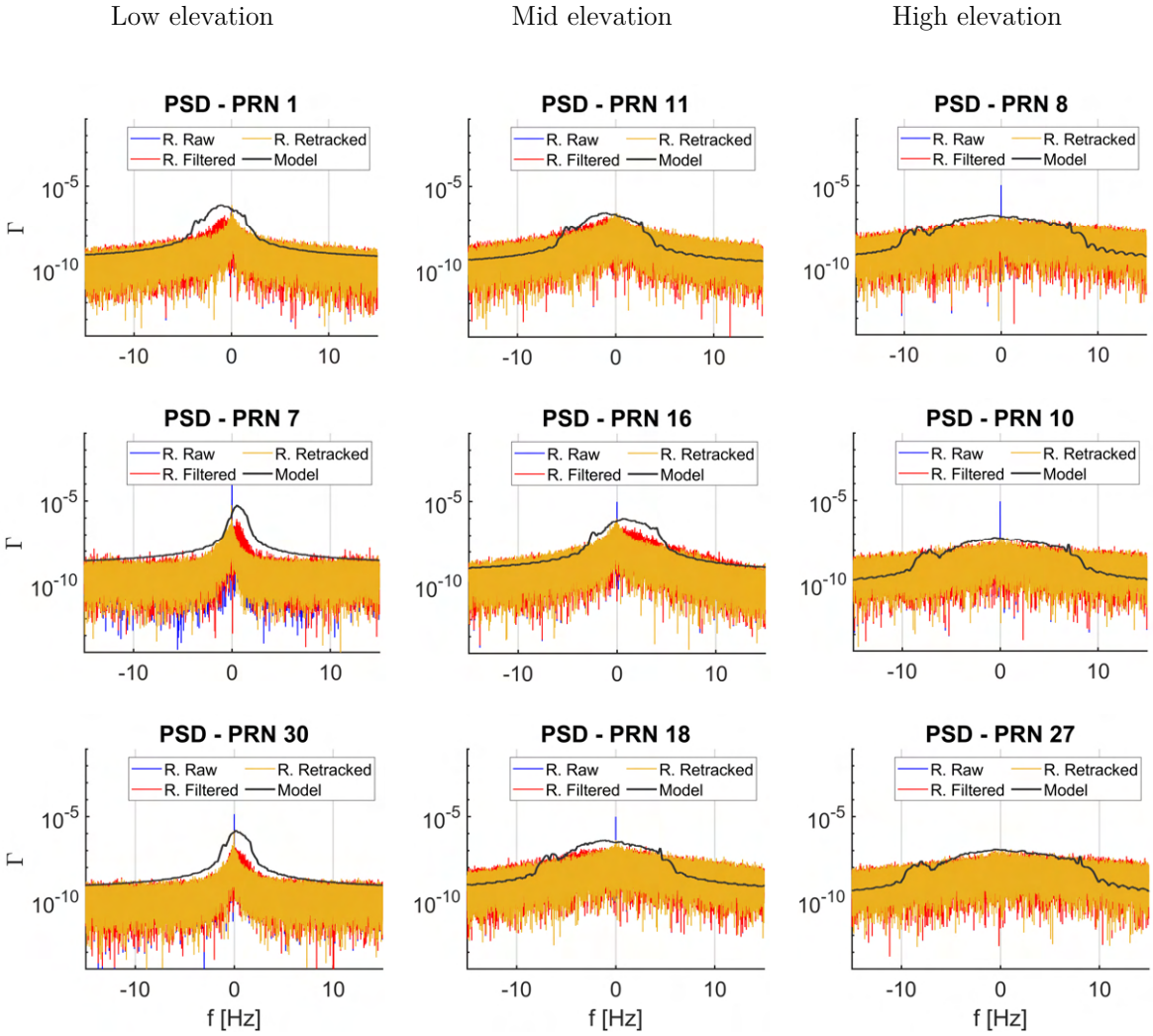

Figure 4.8: Spectrums for events at low, mid, and high elevations on 2019-07-17. At high elevation events, there is no evidence of a defined peak in the modeled or observed power.

A loss of power can be observed on 19 July compared to 17 July, most evident in low elevation events. Although the spectrums of PRN 1, 7, and 30 on the two dates present defined peaks, the values on July 19 are smaller and spreader. Therefore, as expected, there is a negative relation between the sea surface roughness and the power of the re-tracked reflected signal.

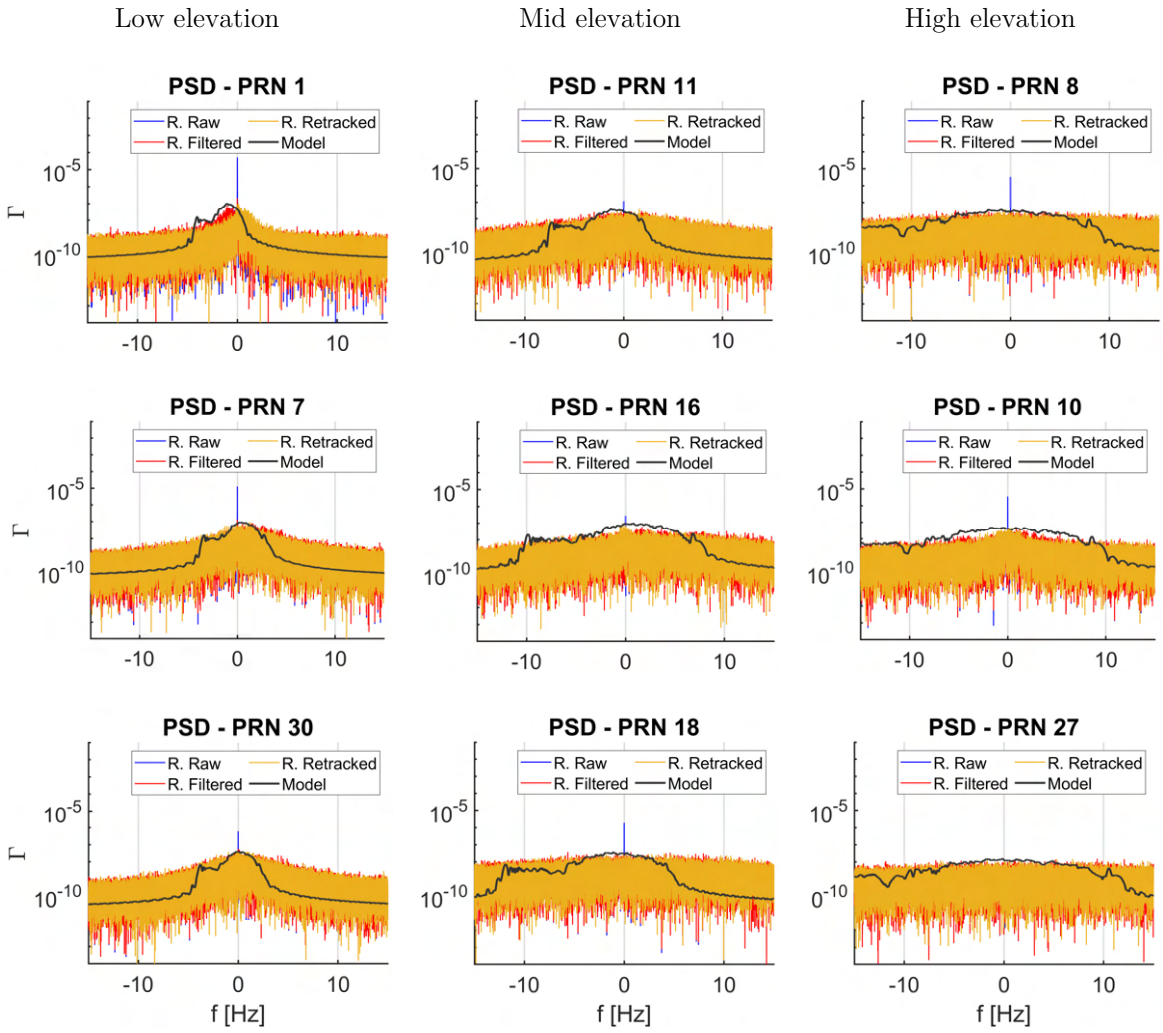

Figure 4.9: Spectrums for events at low, mid, and high elevations on 2019-07-12. At elevation events, there is no evidence of a defined peak in the modeled or observed power.

From the PSD analysis, events in which the model and observed signal did not present coherent reflection, i.e., an identifiable peak, are considered in the noise level, and therefore they are excluded for the subsequent analysis. Specular reflection depends on elevation angles and surface roughness. The excluded events are mainly those at high elevation angles and those in the mid-elevation angles range in cases where the sea surface roughness did not allow specular reflection.

4.2.2 Observed Reflectivity

Reflectivity is the parameter that can be described as the amount of power from the reflected signal with respect to the amount of power received from the direct signal. From the spectral approach processed every minute, the observed reflectivity is computed by using the power peaks of the raw complex direct signal and the re-tracked reflected signal, $\max(\Gamma^{\mathrm{D}})$ and $\max(\Gamma^{\mathrm{R}})$, respectively. The observed reflectivity R_o in decibels $[dB]$ evaluated in time T is given by

$$R_o = \ 10 \cdot \log_{10} \left[\frac{\max(\Gamma^{\mathrm{R}})}{\max(\Gamma^{\mathrm{D}}\ )} \right]_{T_a}^{T_b} \tag{4.2}$$

Figure 4.10 presents the spectrum on 2019-07-17 at low elevation events with the direct and reflected peaks every minute marked in the left column. The zoomed section is presented in the right column. It contains the specific location of the direct and reflected signal peaks and Doppler frequency shift f, respectively. By presenting the direct and the reflected spectrums it can be seen, first, the power loss of the reflected signal with respect to the direct signal, and second, the correction of the Doppler frequency shift shown in the x-axis. The direct signal peaks are almost aligned and close to the zero-frequency value. On the other hand, peaks of the reflected re-tracked signal are sparse and apart from the zero frequency.

From this analysis, a bias can be evidenced not only in the power of the reflected signal but also in the Doppler frequency shift observation. In Section 4.2.4 a complete analysis of the Doppler observation is realized.

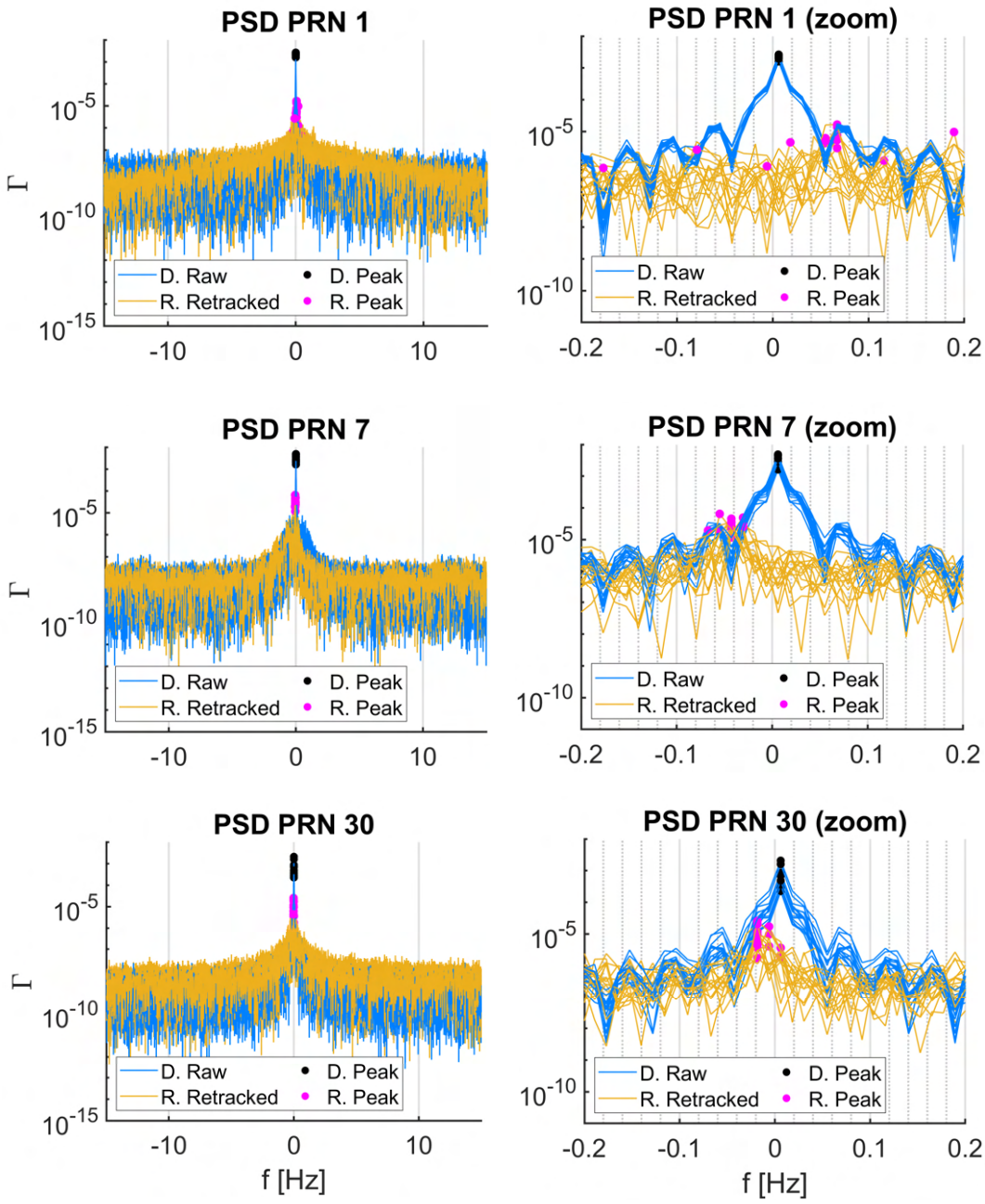

Figure 4.10: Spectrum on 2019-07-17 at low-elevation events. **(Left)** The spectrum of direct tracked signal and reflected re-tracked signal with respective peaks every minute. **(Right)** Zoomed section of spectrums to identify the corresponding location of the peaks in the frequency domain.

Reflectivity vs. the elevation angle is plotted in Figure 4.11. Dates 2019-07-17 (dots) and 2019-07-19 (stars) are selected for the comparison of low and high sea state conditions, ~2.92 m/s (0.26m) and ~6.5 m/s (0.55m) wind speed (SWH), respectively (see Table 3.1). Modeled ocean surface reflectivity is represented by the black line. On 2019-07-17 (low sea state) satellites at low and mid-elevation angles are closer to the modeled reflectivity. High elevation satellites are above the established modeled values out of the limit of specular reflection. Due to the sea state condition on 2019-07-19 (rougher sea surface), the reflectivity is noticeably lower for those events.

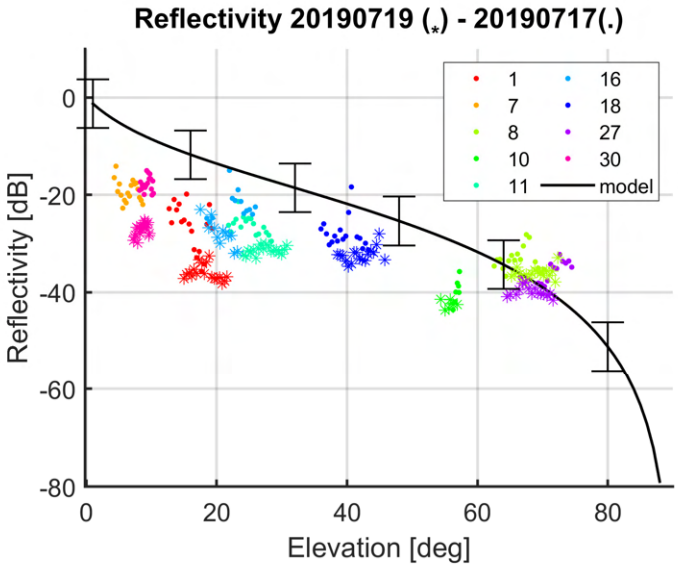

Figure 4.11: Reflectivity vs. Elevation angles on 2019-07-19 (stars) and 2019-07-17 (dots). Both days maintain a similar reflectivity-elevation relation with lower values on 2019-07-19 due to rougher surface.

To represent the results georeferenced on the sea surface, time synchronization is utilized making a join with the modeled specular point position. To ensure only water surface reflections, a land mask is applied as described in section 4.1.1. It removes all modeled reflection points located on the land surface. Map with the reflectivity points located on sea surface on 2019-07-17 and 2019-07-19 are shown in Figure 4.12 and Figure 4.13, respectively. On 2019-07-17, modeled specular points cover distances from ~250m (PRN 10) to ~8000m (PRN 7) from the coastline and up to ~5000m (PRN 30) on 2019-07-19.

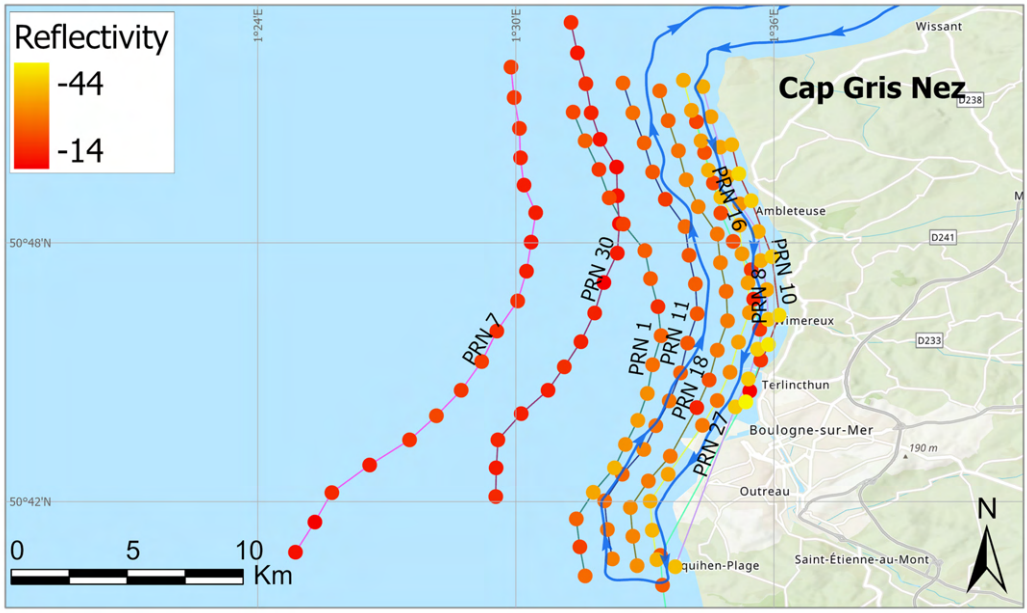

Figure 4.12: Reflectivity [dB] on the modeled specular points positions, located only on the sea surface, on 2019-07-17.

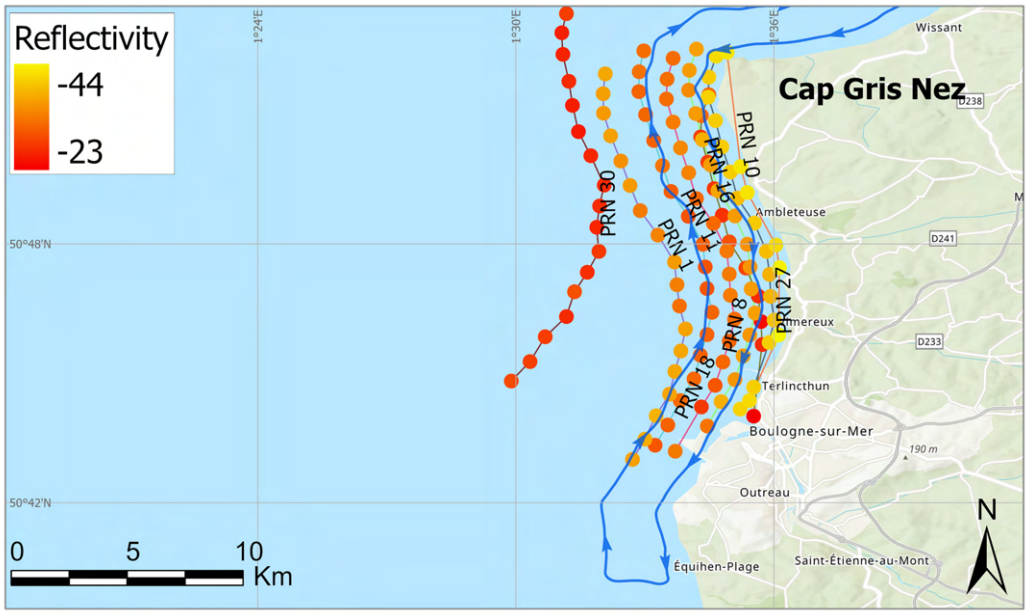

Figure 4.13: Reflectivity [dB] in the modeled specular points, located only on the sea surface, on 2019-07-19.

The reflectivity depends directly on the reflected signal power as specified in eq. (2.9). The latter depends on the transmitter elevation angle and the roughness of the surface as described in eq. (2.7). As expected, on 17 July and 19 July the lowest reflectivity is located on satellites at the high elevation angle, orange, and yellow points in Figure 4.12 and Figure 4.13. Red dots represent higher reflectivity which is found at lower elevation angles. However, the reflectivity on 17 July 2019 is higher ([-24,-14] dB) in comparison with 19 July 2019 ([-34,-24] dB) since the roughness of the sea surface on 17^{th} is the lowest reported in terms of wind speed and significant wave height, during the campaign of data collection.

To determine the correlation between the power of the reflected signal and the ancillary sea state parameters it is necessary to establish a parameter that shows the bias between the observed quantities and the expected (modeled) quantities. The explanation of this parameter and the correlation results are described in the following section.

4.2.3 Correlation Sea State Factor and Sea State

The reduction of the observed reflectivity R_o using the computed reflectivity R_c in eq. (2.9), provides a residual. The latter will be called the sea state factor (SSF). This parameter is used to evaluate the correlation between the reflectivity obtained from the analysis of the power observations, with respect to the ancillary sea state parameters. The SSF reads

$$SSF = R_o - R_c \tag{4.3}$$

SSF values above zero exceed the specular reflection model, i.e., the incoherent component in the reflection process starts to dominate. These events are primarily found at high elevation angles. The sea state factor also decays as the sea state on the different dates of data collection increases. Figure 4.14 presents the sea state factor results grouped by date. In agreement with reflectivity results, SSF values on 17 July 2019 are the highest in comparison with the other dates.

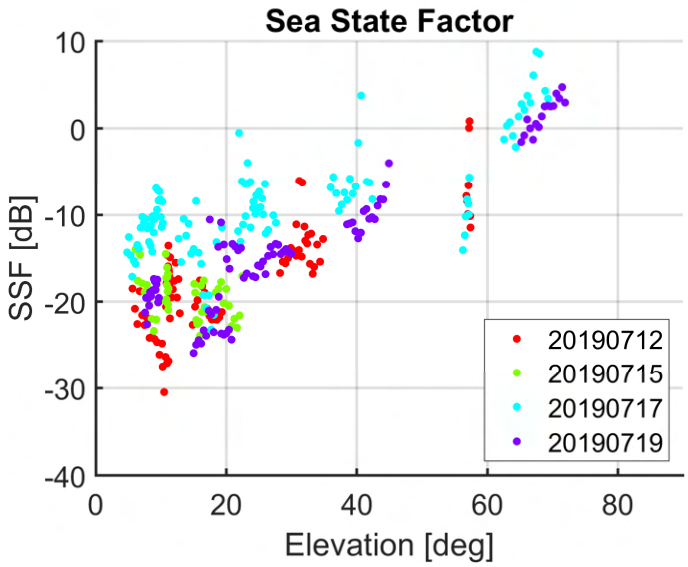

Figure 4.14: Sea state factor at different elevation angle events grouped by date of data collection. Cian dots (2019-07-17) are close to zero which means the higher reflect signal power due to the low sea state.

Wind speed and significant wave height from the ERA5 model are stored in raster format (*GeoTIFF*) with a spatial resolution of 18 km and 25 km, respectively. A geo-interpolation depending on pixel value and localization is used to extract the pixel values at the specular point positions to smooth the respective parameter retrieval. Figure 4.15 and Figure 4.16 show SSF versus WS and SWH, respectively.

(a)

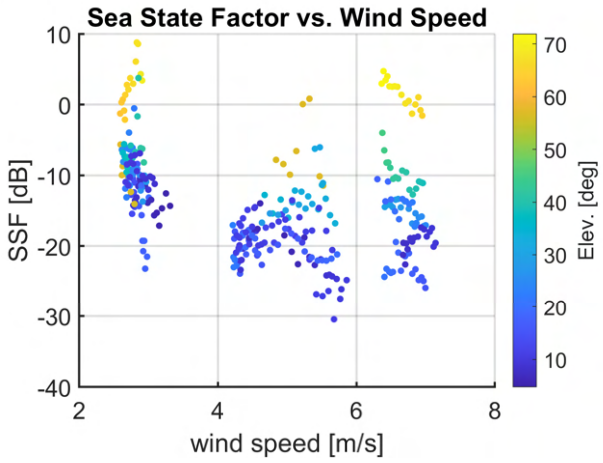

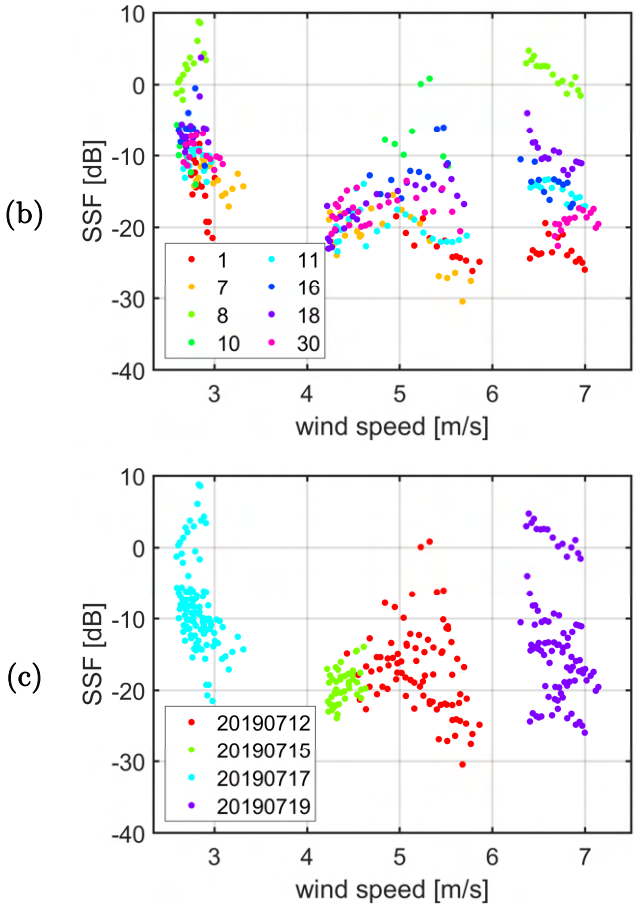

Figure 4.15: Sea state factor vs wind speed from ERA5 model. **(a)** including elevation angles. **(b)** grouped by PRN. **(c)** grouped by date of measurements.

As mentioned in section 2.2.2 specular reflection is present at low elevation angles (high incident angles) and surfaces with low roughness. The blowing of the wind is one of the parameters linked to the sea waves. So, the wind speed is directly proportional to the waves generated. Therefore, the higher the wind speed the higher the roughness of the sea surface. As can be observed in Figure 4.15, the power loss of the reflected signal represented by the SSF agrees with the wind speed retrieved from the ERA5 model since the latter increases the sea state. The SSF values at the lowest sea state are concentrated around -10 dB. Whereas at the higher sea states, the values are spread and can decay up to -30 dB.

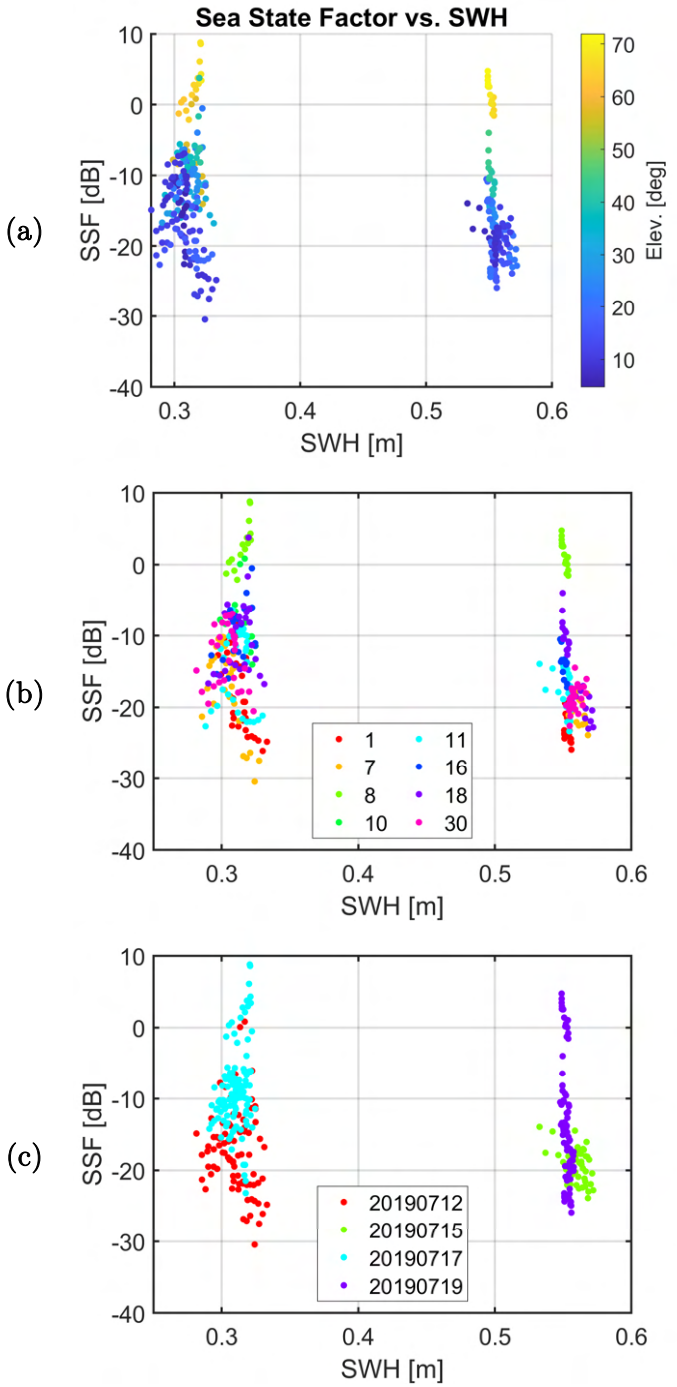

Figure 4.16: Sea state factor vs SWH from ERA5 model. **(a)** including elevation angles. **(b)** grouped by PRN. **(c)** grouped by date of measurements.

Values of the SFF with respect to the significant wave height present the same behavior as for the wind speed. The higher the SWH, the higher the loss of the power of the reflected signal. However, the events are less spread in comparison with the values of the wind speed. This effect is primarily caused by the different spatial resolution between the raster of the WS and SWH. The latter contains bigger pixels (25 km x 25 km), so the interpolated values in the specular points are similar at contiguous locations.

A bivariate map of sea state factor variability with respect to elevation angle change is shown in Figure 4.17. A color scale is given for each variable, pink for SSF, and blue for elevation. The combination of both the square color scale is generated. Then, high elevation values with high (negative) SSF values are represented by dark blue, and low elevation with low (negative) SFF are represented by light pink.

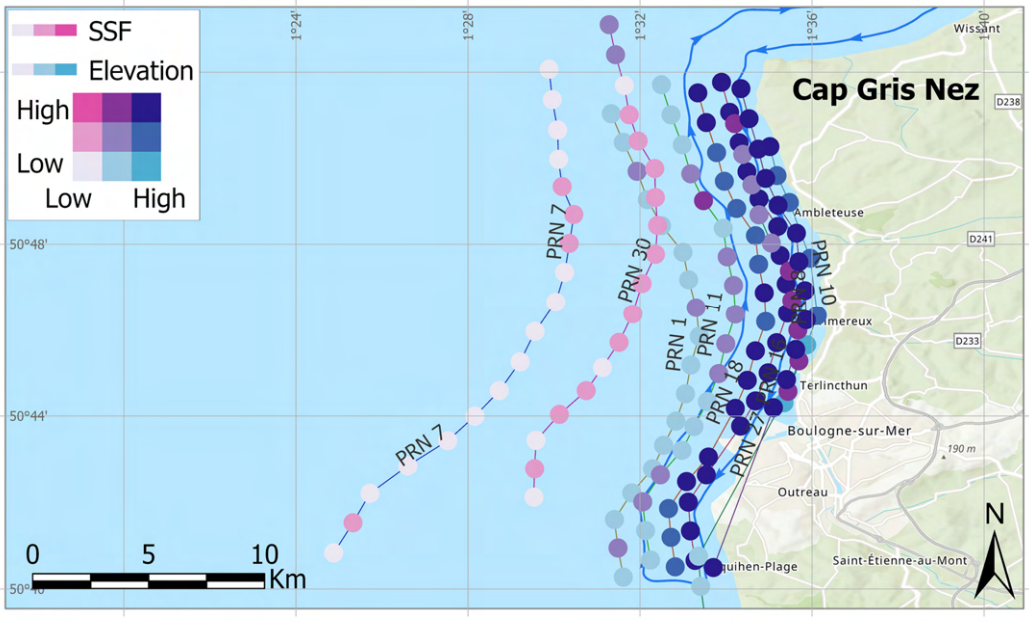

Figure 4.17: Map of SSF variability with respect to elevation angle change. At high elevation angles, are found highest (negative) sea state factor.

The Pearson correlations are computed at different elevation angles ranges to distinguish the behavior of the events with respect to the elevation angle changes. Events are categorized as Low: $E < 10°$, mid: $10° < E < 30°$, and high: $E > 30°$ and the results are shown in Table 4.1.

Parameter	SSF – Low $E < 10°$	SSF – Mid $10° < E < 30°$	SSF – High $E > 30°$
Wind speed	-0.7346	-0.4639	-0.1221
SWH	-0.5066	-0.3775	-0.0007

Table 4.1: Correlations sea state factor and wind speed and significant wave height.

The correlation table contains the events including all the dates of data collection selected from the reflection response analysis. The sea state factor has a high and moderate Pearson anti-correlation to wind speed and SWH, respectively. The anti-correlation was expected since the increase of the sea state causes a decrease in the power of the reflected re-tracked signal and vice versa. Besides, it can be observed the expected effect with respect to the elevation angles as well. The highest anti-correlation is found at events with low elevation angles. The anti-correlation decreases as the elevation angles increase and events in the high elevation range do not correlate with the sea state factor.

4.2.4 Correlation Doppler Shift and Sea State

Doppler frequency shift information has been analyzed in GNSS-R for ocean altimetry and surface ocean roughness (wind velocity parameter) (e.g. [Semmling et al., 2013; Semmling, M., 2012]). As described in section 4.2.1, the PSD approach allows obtaining the Doppler frequency shift f from the position of the maximum peak of the Fourier transform Γ at the specific time interval. As shown in Figure 4.18, at a low sea state (2019-07-17), the Doppler shift variations are low around the zero value. In contrast, at a higher sea state, the variation increases considerably.

To analyze the Doppler shift variations, the Doppler distribution is calculated. The latter is represented by the Doppler shift mean presented in Table 4.2, and The Doppler shift standard deviation, in Table 4.3.

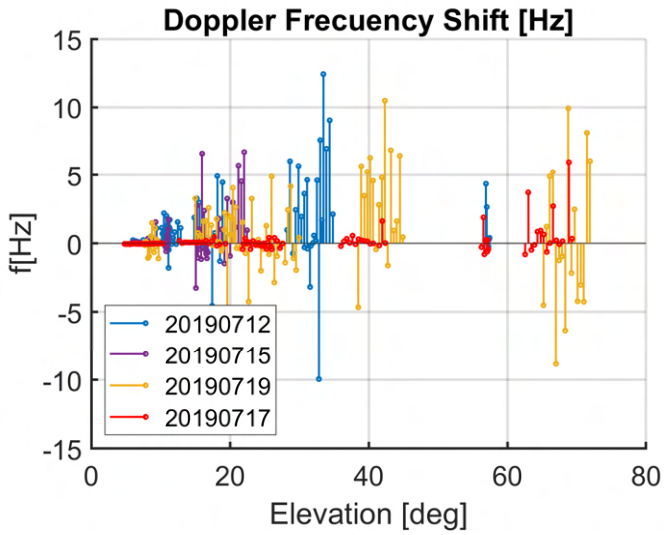

Figure 4.18: Doppler Frequency shift vs. elevation angles grouped by date. Doppler distribution has a dependency on elevation angles and sea surface roughness.

Results reveal the sensitivity of the Doppler shift observable with respect to sea state and elevation angle. The Doppler shift mean and standard deviation are considerably lower on 17 July 2019 than the other dates and they increase at the presence of a higher sea state, and high elevation angle.

Date	Mean Doppler [Hz] $E < 10°$	Mean Doppler [Hz] $10° < E < 30°$	Mean Doppler [Hz] $E > 30°$
20190712	0.2188	0.9566	1.8949
20190715	0.2459	0.8839	~
20190717	-0.0301	-0.0058	0.4509
20190719	-0.0649	0.5722	1.7262

Table 4.2: Mean of the Doppler shift at different elevation angles of events grouped by day regardless of the PRN. High elevation events on 2019-07-15 are excluded from the PSD analysis.

Date	STD Doppler [Hz] $E < 10°$	STD Doppler [Hz] $10° < E < 30°$	STD Doppler [Hz] $E > 30°$
20190712	0.2909	1.8742	4.2486
20190715	0.4437	2.2183	~
20190717	0.0174	0.2041	1.2998
20190719	0.7181	2.0394	4.9026

Table 4.3: Standard deviation of Doppler shift at different elevation angles of events grouped by day regardless of the PRN. High elevation events on 2019-07-15 are excluded from the PSD analysis.

Figure 4.19 the bivariate map of the Doppler shift variability at different elevation angles located along with the segment analysis from Cap Gris Nez to Equihen-Plague. As similar to the bivariate map of SFF and elevation angles, a color scale is given for each variable, pink for Doppler frequency shift, and blue for elevation angles. Then, high elevation values with high Doppler frequency shift values are represented by dark blue, and low elevation with low Doppler frequency shifts are represented by light pink.

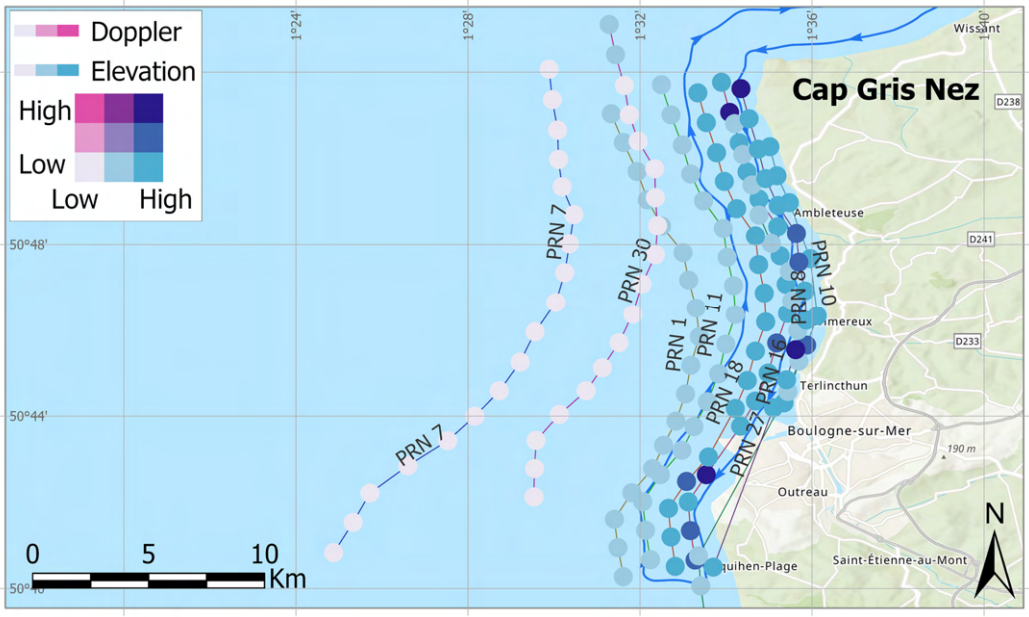

Figure 4.19: Map of Doppler shift variability with respect to elevation angle change on 2017-07-17. At low elevation angles, low Doppler shift, and vice versa.

To establish the correlation with the sea state parameters, a measure of the variation of the Doppler shift for each event is used. It is computed the standard deviation of the Doppler shift retrievals for each PRN along the North-south segment as follows

$$\sigma_f^j = \sqrt{\frac{1}{N}\sum_{i=1}^{N}(f_i - \mu)^2} \tag{4.4}$$

The superscript j indicates the PRN, subscript i each value retrieved of the Doppler frequency shift, N total number of values, and μ the mean value of the set. The Pearson correlation is computed for low, mid, and high elevation angle events. Table 4.4 shown the correlation results.

Parameter	STD Doppler [Hz] $E < 10°$	STD Doppler [Hz] $10° < E < 30°$	STD Doppler [Hz] $E > 30°$
Wind speed	0.9421	0.6395	0.6080
SWH	0.8530	0.6061	0.5691

Table 4.4: Correlations of the standard deviation of the Doppler frequency shift and wind speed and significant wave height.

The correlation table contains the events including all the dates of data collection selected from the reflection response analysis. The standard deviation of the Doppler shift has a very high positive Pearson correlation with respect to wind speed and SWH. The positive correlation denotes that an increase in the sea state causes an increase in the Doppler shift variations as presented in Figure 4.18. The Doppler shift standard deviation and sea state parameters correlations are also sensitive to the transmitter elevation angles. The highest correlation is found at low elevation angles and the correlation decreases significantly for events with elevations above 10°. Standard deviation Doppler shift events in the mid and high elevation range have a moderate correlation with respect to sea state parameters without significant correlation changes in those elevation ranges events.

5 Conclusions and Outlook

Coastal areas are among the locations most affected by sea level rise and sea state variability caused by climate change and global warming. This Master's thesis has presented an approach to monitor sea state parameters in those zones by using the signals broadcasted by GNSS satellites as signals of opportunity. Previous studies revealed promising results employing GNSS reflectometry in sea state retrievals on a static ground-based configuration in coastal and space-borne experiments under certain conditions by analyzing the reflected signal on open sea surface tracks. This experiment used low-altitude airborne measurements to determine the sensitivity of the reflected signal to sea state changes. In this approach, the tracking of the direct signal allowed us to estimate its power through to the in-phase component. Besides, the re-tracking process, aided by the modeled path difference, allowed us to estimate the power of the reflected signal. From the direct and reflected signal power, it is possible to derive the sea state factor (observed minus computed reflectivity), and the Doppler shift distribution (mean and standard deviation) from which the Pearson correlation with ancillary sea state data could be determined.

Results have shown that there is a correlation between the reflectometry retrievals and sea state parameters from ERA5, therefore it is feasible to retrieve sea state (surface roughness) from airborne GNSS-R measurements in coastal zones. The power of the reflected signal allowed us to derive the sea state factor. The latter has a high and moderate degree of anti-correlation with WS and SWH depending on the elevation angle, respectively. The highest anti-correlations are found at low elevation angles (here categorized as $E < 10°$) with values of, -0.73 and -0.51 for WS and Shaw, respectively. The correlation degree decreased significantly as the elevation angle of the transmitter increased, showing agreement with the specular reflection model where the coherent reflection component vanished at high elevations.

Besides the elevation angle dependency, low, moderate, and high sea states are analyzed as well. On 17 July 2019, the lowest sea state is reported (WS: 2.92 m/s, SWH: 0.26 m) corresponding to a Doppler shift mean of -0.03 Hz and 0.45 Hz at low and high elevations, respectively. Whereas on 12 July 2019 (WS: 5.49 m/s, SWH: 0.30 m), 0.22 Hz and 1.89 Hz are obtained at low and high elevations angles. Therefore, the sensitivity of the Doppler frequency shift with respect to sea surface roughness from airborne measurements could be evidenced. The

Doppler shift standard deviation presented a high degree correlation with respect to wind speed and significant wave height is also sensitive to the elevation angle changes. The highest correlation results are obtained at a low elevation angle ($E < 10°$). Doppler shift standard deviation and wind speed have a Pearson correlation of 0.94 and 0.85 for SWH, decreasing when the elevation angle increases.

The up-looking antenna and receiver setup has a good performance for experimental purposes. Although on some days it was not possible to obtain data from RHCP or LHCP signals due to recording failures, the independent single front-end receivers worked as a backup system that allowed us to have at least one data set for the respective polarized signal. Only the signals from the dedicated RHCP receiver are analyzed in this project. Further work would consist of analyzing the signals from the LHCP receiver and comparing their results against RHCP signals results. Additionally, the antenna gain pattern correction, neglected in this study, needs to be analyzed. When receiving signals from multiple directions and satellites simultaneously, the gain pattern, phase center, and multipath suppression become important characteristics to correctly discriminate useful signals to process and differentiate them from the noise level.

The selected platform turned out to be a notable option in terms of performance. The gyrocopter allowed stable flights with trajectories closely aligned with the flight plan designed for the experiment, which facilitated the analysis of very similar sections during different days of data collection. Some satellite signals are lost along certain sections of the flight trajectory, especially at the points where strong changes in the sight direction of the gyrocopter occurred. These signal losses can be attributed mainly to changes in the orientation of the antenna and the frame of the aircraft blocking the signal. A different antenna setup can be implemented in this platform for new experiments, e.g., a down-looking or side-looking antenna or two or more antennas in a master-slave configuration for direct and reflected signals.

The flight design allowed us to perform different analyses in the experiment. Although the east-west section of the trajectory also presented a reflectivity response based on DDM retrievals, the greatest response occurred in the north-south section attributed to transmitter-specular point-receiver geometry, the sight angle of the gyrocopter (antenna orientation), and major availability of visible satellites than the available in the North direction. The east-west section may also be analyzed to determine the behavior of the sea state factor and

Doppler distribution since the wind direction and speed in that location leads to a different sea state. The designed flight trajectory also allowed us to retrieve reflection events up to ~7 km from the coastline in the north-south segment. The analysis of the back leg (south-north) would extend the range of the reflection tracks from the coastline and would increase the data collected nearby.

This master thesis presented the sensitivity of the power and Doppler frequency shift of the reflected GNSS signals with respect to the sea surface roughness, which offers the possibility of monitoring the sea state in coastal areas. However, there are further aspects that could be considered to establish a methodology that allows characterization of the sea surface from airborne measurements with sufficient accuracy that could be extended to space-borne data.

The transmitter, specular point, and receiver positions are essential factors in GNSS-R for precise results. In this project, the position of the receiver is obtained with a stand-alone positioning method and the transmitter location is obtained by broadcasted ephemeris. Obtaining the receiver position by a differential or precise point positioning method (PPP) will increase the accuracy and reduce the biases in the models used. Furthermore, the analysis of height fluctuations and aircraft attitude could be carried out to understand the effects of these parameters on airborne GNSS-R when retrieving the sea state.

Tropospheric and ionospheric corrections are neglected in this study. A complete study applying bent propagations corrections for airborne experiments similar to the presented in Semmling et al., [2013] (for altimetry) is needed. It would provide an improved understanding of the tropospheric and ionospheric effects on reflected signals to characterize the roughness of the sea surface by implementing more precise reflection models. These studies could then be scaled to space-borne measurements. As presented in Cardellach et al., [2020], coherent reflections from spaceborne reflectometry (CYGNSS data) have certain behaviors that could have been caused by ionospheric scintillation phenomena. However, it is still an open topic that requires further studies and analyses.

Based on the results, a variation in Doppler frequency shift could be observed on days with similar wind speed or SWH but with different wind directions. The latter is an important component of the sea state in coastal areas. Therefore, future work could be focused on determining the correlation and influence of the wind direction with Doppler retrievals from GNSS-R and establish models to derive this parameter from airborne data.

Bibliography

Alonso-Arroyo, A., Camps, A., Park, H., Pascual, D., Onrubia, R., & Martin, F. (2015). Retrieval of Significant Wave Height and Mean Sea Surface Level Using the GNSS-R Interference Pattern Technique: Results From a Three-Month Field Campaign. *IEEE Transactions on Geoscience and Remote Sensing*, *53* (6), 3198–3209. https://doi.org/10.1109/TGRS.2014.2371540

Bacci, G., Falletti, E., Fernández-Prades, C., Luise, M., Margaria, D., & Zanier, F. (2012). Chapter 2—Satellite-Based Navigation Systems. In D. Dardari, E. Falletti, & M. Luise (Eds.), *Satellite and Terrestrial Radio Positioning Techniques* (pp. 25–74). Academic Press. https://doi.org/10.1016/B978-0-12-382084-6.00002-7

Beckheinrich, J., Beyerle, G., Schön, S., Apel, H., Semmling, M., & Wickert, J. (2012). WISDOM: GNSS-R based flood monitoring. *2012 Workshop on Reflectometry Using GNSS and Other Signals of Opportunity (GNSS+R)*, 1–6. https://doi.org/10.1109/GNSSR.2012.6408257

Beckmann, P., & Spizzichino, A. (1987). *The Scattering of Electromagnetic Waves from Rough Surfaces*. Artech Print on Demand.

Bengtsson, L., Hodges, K. I., & Roeckner, E. (2006). Storm Tracks and Climate Change. *Journal of Climate*, *19* (15), 3518–3543. https://doi.org/10.1175/JCLI3815.1

Benveniste, J., Cazenave, A., Vignudelli, S., Fenoglio-Marc, L., Shah, R., Almar, R., Andersen, O., Birol, F., Bonnefond, P., Bouffard, J., et. al., (2019). Requirements for a Coastal Hazards Observing System. *Frontiers in Marine Science*, *6*. https://doi.org/10.3389/fmars.2019.00348

Cardellach, E., Li, W., Rius, A., Semmling, M., Wickert, J., Zus, F., Ruf, C. S., & Buontempo, C. (2020). First Precise Spaceborne Sea Surface Altimetry With GNSS Reflected Signals. *IEEE Journal of Selected Topics in Applied Earth Observations and Remote Sensing*, *13*, 102–112. https://doi.org/10.1109/JSTARS.2019.2952694

Cazenave, A., & Cozannet, G. L. (2014). Sea level rise and its coastal impacts. *Earth's Future*, *2* (2), 15–34. https://doi.org/10.1002/2013EF000188

Circular polarization. (2020). In *Wikipedia*. https://en.wikipedia.org/w/index.php?title=Circular_polarization&oldid=992332190

Dana, P. H. (1998). *The Global Positioning System* (Educational). https://foote.geography.uconn.edu/gcraft/notes/gps/gps_f.html

Darrozes, J., Roussel, N., & Zribi, M. (2016). The Reflected Global Navigation Satellite System (GNSS-R): From Theory to Practice. In N. Baghdadi & M. Zribi (Eds.), *Microwave Remote Sensing of Land Surface* (pp. 303–355). Elsevier. https://doi.org/10.1016/B978-1-78548-159-8.50007-4

Ebinuma, T., & Yasuda, A. (2010). Airborne GPS Reflectometry from Low Altitude Aircraft. *SICE Journal of Control, Measurement, and System Integration*, *3* (6), 429–434. https://doi.org/10.9746/jcmsi.3.429

ESA Climate Office. (2020). *Sea state*. ESA Climate Office. https://climate.esa.int/en/projects/sea-state/

Hofmann-Wellenhof, B., Lichtenegger, H., & Collins, J. (2001). *Global Positioning System: Theory and Practice* (5th ed.). Springer-Verlag. https://doi.org/10.1007/978-3-7091-6199-9

Hofmann-Wellenhof, B., Lichtenegger, H., & Wasle, E. (2008). *GNSS - Global Navigation Satellite Systems, Original text: GPS, GLONASS, Galileo, and more*. Springer-Verlag. https://doi.org/10.1007/978-3-211-73017-1

Hoseini, M., Semmling, M., Nahavandchi, H., Rennspiess, E., Ramatschi, M., Haas, R., Strandberg, J., & Wickert, J. (2020). On the Response of Polarimetric GNSS-Reflectometry to Sea Surface Roughness. *IEEE Transactions on Geoscience and Remote Sensing*, 1–12. https://doi.org/10.1109/TGRS.2020.3031396

IEEE Standard. (2016). IEEE Standard for Radar Definitions. *IEEE P686/D2, October 2016*, 1–55.

Jin, S., Cardellach, E., & Xie, F. (2014). *GNSS Remote Sensing: Theory, Methods and Applications*. Springer Netherlands. https://doi.org/10.1007/978-94-007-7482-7

Kleusberg, A., & Teunissen, P. J. G. (Eds.). (1996). *GPS for Geodesy*. Springer-Verlag. https://doi.org/10.1007/BFb0117676

Kucwaj, J.-C., Reboul, S., Stienne, G., Choquel, J.-B., & Benjelloun, M. (2017). Circular regression applied to GNSS-R phase altimetry. *Remote Sensing*, *9*. https://doi.org/10.3390/rs9070651

Lee, Y.-L., Pan, J., Hathaway, R. B., & Barkey, M. E. (2005). *Fatigue Testing and Analysis*. Butterworth-Heinemann. https://doi.org/10.1016/B978-075067719-6/50011-7

Marchán, J., Rodriguez-Alvarez, N., Camps, A., Bosch, X., Ramos-Perez, I., & Valencia, E. (2008). Correction of the Sea state Impact in the L-Band Brightness Temperature by Means of Delay-Doppler Maps of Global Navigation Satellite Signals Reflected Over the Sea Surface. *Geoscience and*

Remote Sensing, IEEE Transactions On, *46*, 2914–2923. https://doi.org/10.1109/TGRS.2008.922144

Martín-Neira, M. (1993). A Passive Reflectometry and Interferometry System (PARIS): Application to ocean altimetry. *ESA Journal*, *17*, 331–355.

Melet, A., Teatini, P., Le Cozannet, G., Jamet, C., Conversi, A., Benveniste, J., & Almar, R. (2020). Earth Observations for Monitoring Marine Coastal Hazards and Their Drivers. *Surveys in Geophysics*, *41* (6), 1489–1534. https://doi.org/10.1007/s10712-020-09594-5

NASA, G. C. (2020). *Sea Level | NASA Global Climate Change*. Climate Change: Vital Signs of the Planet. https://climate.nasa.gov/vital-signs/sea-level

Nievinski, F. G., & Larson, K. M. (2014). Forward modeling of GPS multipath for near-surface reflectometry and positioning applications. *GPS Solutions*, *18* (2), 309–322. https://doi.org/10.1007/s10291-013-0331-y

Park, J., Johnson, J. T., O'Brien, A., & Lowe, S. T. (2016). Studies of TDS-1 GNSS-R ocean altimetry using a "full DDM" retrieval approach. *2016 IEEE International Geoscience and Remote Sensing Symposium (IGARSS)*, 5625–5626. https://doi.org/10.1109/IGARSS.2016.7730469

Sanz Subirana, J., Zornoza, J., & Hernandez-Pajares, M. (2011). *GNSS signal—Navipedia*. ESA Navipedia. https://gssc.esa.int/navipedia/index.php/GNSS_signal

Scharf, L. L., & Schreier, P. J. (Eds.). (2010). The origins and uses of complex signals. In *Statistical Signal Processing of Complex-Valued Data: The Theory of Improper and Noncircular Signals* (pp. 3–29). Cambridge University Press. https://doi.org/10.1017/CBO9780511815911.003

Semmling, M., Beckheinrich, J., Wickert, J., Beyerle, G., Schön, S., Fabra, F., Pflug, H., He, K., Schwabe, J., & Scheinert, M. (2014). Sea surface topography retrieved from GNSS reflectometry phase data of the GEO-HALO flight mission. *Geophysical Research Letters*, *41* (3), 954–960. https://doi.org/10.1002/2013GL058725

Semmling, M., Beyerle, G., Stosius, R., Dick, G., Wickert, J., Fabra, F., Cardellach, E., Ribó, S., Rius, A., Helm, A., Yudanov, S. B., & d'Addio, S. (2011). Detection of Arctic Ocean tides using interferometric GNSS-R signals. *Geophysical Research Letters*, *38* (4). https://doi.org/10.1029/2010GL046005

Semmling, M., Schmidt, T., Wickert, J., Schön, S., Fabra, F., Cardellach, E., & Rius, A. (2012). On the retrieval of the specular reflection in GNSS

carrier observations for ocean altimetry. *Radio Science*, *47* (6). https://doi.org/10.1029/2012RS005007

Semmling, M., Wickert, J., Schön, S., Stosius, R., Markgraf, M., Gerber, T., Ge, M., & Beyerle, G. (2013). A zeppelin experiment to study airborne altimetry using specular global navigation satellite system reflections. *Radio Science*, *48* (4), 427–440. https://doi.org/10.1002/rds.20049

Semmling, M., Wickert, J., Schön, S., Stosius, R., Markgraf, M., Gerber, T., Ge, M., & Beyerle, G. (2013). A zeppelin experiment to study airborne altimetry using specular Global Navigation Satellite System reflections. *Radio Science*, *48*, 427–440. https://doi.org/10.1002/rds.20049

Semmling, M. (2012). *Altimetric monitoring of Disko Bay using interferometric GNSS observations on L1 and L2*, volume Scientific Technical Report STR12/04. Deutsches GeoForschungsZentrum GFZ Potsdam. https://doi.org/10.2312/GFZ.b103-12049

Semmling, M., Beyerle, G., Beckheinrich, J., Ge, M., & Wickert, J. (2014). Airborne GNSS reflectometry using crossover reference points for carrier phase altimetry. *2014 IEEE Geoscience and Remote Sensing Symposium*, 3786–3789. https://doi.org/10.1109/IGARSS.2014.6947308

United Nations. (2017). *Ocean Conference. United Nations. 2017*. https://www.un.org/sustainabledevelopment/wp-content/uploads/2017/05/Ocean-fact-sheet-package.pdf

Wickert, J. (2019). *GNSS Reflectometry*. Technical University Berlin, Lecture Presentation.

Xu, G., & Xu, Y. (2016). *GPS: Theory, Algorithms and Applications* (3rd ed.). Springer-Verlag. https://doi.org/10.1007/978-3-662-50367-6

Zavorotny, V. U., Larson, K. M., Braun, J. J., Small, E. E., Gutmann, E. D., & Bilich, A. L. (2010). A Physical Model for GPS Multipath Caused by Land Reflections: Toward Bare Soil Moisture Retrievals. *IEEE Journal of Selected Topics in Applied Earth Observations and Remote Sensing*, *3* (1), 100–110. https://doi.org/10.1109/JSTARS.2009.2033608

Zavorotny, V. U., & Voronovich, A. G. (2000). Scattering of GPS signals from the ocean with wind remote sensing application. *IEEE Transactions on Geoscience and Remote Sensing*, *38* (2), 951–964. https://doi.org/10.1109/36.841977

Ziedan, N. I. (2006). *GNSS Receivers for Weak Signals*. Artech House. ISBN: 1596930527